CURVATURE-DIRECTED CRYSTALLIZATION OF POLYMER DIELECTRICS IN NANOPORES

A Thesis

by

DARIYA KONSTANTINOVNA REID

Submitted to the Office of Graduate and Professional Studies of
Texas A&M University
in partial fulfillment of the requirements for the degree of

MASTER OF SCIENCE

Chair of Committee,	Jodie L. Lutkenhaus
Committee Members,	Sam Mannan
	Hung-Jue Sue
Head of Department,	Nazmul Karim

December 2013

Major Subject: Chemical Engineering

ABSTRACT

The formation of isotactic poly(propylene) (iPP) and polycarbonate (PC) nanowires of tunable diameter was demonstrated by melt-wetting the polymer into nanoporous anodic alumina. The crystallization process was analyzed using differential scanning calorimetry. A transition from hetero- to homogeneous crystallization was observed for iPP as the pore diameter decreased. Also, the Avrami exponent decreased as the pore diameter decreased, indicating preferential 1-D crystallization for diameters of 40 nm or less. X-ray diffraction studies showed that the polymer chains crystallize into the α-phase and that they preferentially orient along the a- and b-axis, perpendicular to the pore wall. Directed crystallization of iPP may enhance the materials electrical and mechanical properties.

ACKNOWLEDGEMENTS

I would like to thank my advisor, Dr. Lutkenhaus, for the support and patience she has shown in teaching me and guiding my research work. I also wish to thank Dr. Mannan and Dr. Sue for serving on my committee and for guidance in completing my project.

I would also like to thank my lab mates, past and present, and my friends here at Texas A&M University for their inspiration and support.

NOMENCLATURE

A_{tot}	Total area
AAO	Anodic aluminum oxide
C	Capacitance
C_p	Heat capacity
d	Diameter
d_{hkl}	Interplanar spacing
DSC	Differential scanning calorimetry
E	Applied electric field
H	Heat evolved
H_f	Enthalpy of fusion
iPP	Isotactic polypropylene
k	Crystallization rate constant
l	Pore length
n	Avrami exponent
PC	Polycarbonate
PE	Polyethylene
PEO	Poly(ethylene oxide)
PS	Polystyrene
S	Surface tension
SEM	Scanning electron microscopy

t	Time
T_c	Crystallization temperature
T_g	Glass transition temperature
T_m	Melting temperature
T_m^o	Equilibrium melting temperature
$t_{1/2}$	Half-time of crystallization
U_e	Energy stored
X	Crystalline fraction
γ_{LG}	Liquid-gas surface tension
γ_{SG}	Solid-gas surface tension
γ_{SL}	Solid-liquid surface tension
ε	Dielectric constant
ε_o	Permittivity of free space
θ	Diffraction angle
λ	Wavelength
ρ_s	Density
σ_{SL}	Solid-liquid interface energy
φ	Porosity
Φ	Stability parameter
Ψ	Tilt angle

TABLE OF CONTENTS

Page

LIST OF FIGURES

Page

LIST OF TABLES

Page

1. INTRODUCTION

Capacitors are a basic building block in almost any electronic device. Their main purpose is to provide energy storage and load leveling. Continuing advances in the electronics industry require development of energy storage systems that are smaller and more economical; also, the global energy demand requires systems with higher power and energy density. Improving charge storage will also reduce the amount of energy needed to power electronic devices thus, reducing global oil consumption. As the physical dimensions of electronic devices continue to shrink, advances in capacitors technology are directed at improving the efficiency of the device as well as the device's performance under increased stress. Increasing attention is given to improvements in materials with inherently high capacity for charge storage and materials that will be able to withstand high voltage application.

The basic geometry of a capacitor is two conductive plates separated by a dielectric material. When a voltage is applied across the plates it creates an internal electric field in the dielectric layer, which forces charges to separate and collect on the conducting plates. The energy stored (U_e) is described by the following equation:

$$U_e = \frac{1}{2}\varepsilon\varepsilon_o E^2 \qquad (1)$$

where ε_o is the permittivity of free space, ε is the dielectric constant (or permittivity) of the material, and E is the electric field applied.[1] The focus of this project is the dielectric layer. Key properties for a dielectric material are the break down voltage and the

dielectric constant. The energy density is limited by the break down voltage, which is related to the ultimate electric field before failure. Ceramics are commonly used in capacitors owing to the high dielectric constant of the material, but they have a low break down voltage. On the other hand, polymer dielectrics are of interest because they have a high breakdown voltage relative to ceramics. However, the dielectric constant of most polymers is lower than that of ceramic materials, which limits the energy stored. One method to increase the dielectric constant of the dielectric layer is to add ceramic fillers to form polymer composites. Increase in the concentration of filler is accompanied by an increase in the dielectric constant. Yet, such materials show limited stability under electric fields and some thermal instability.[2] A new method is needed which can alter the structure of polymeric materials in a way that will increase both the dielectric constant and breakdown voltage of the material.

Though there have been other extensive studies done on the effect of confinement on polymer properties, most have concentrated on the properties of thin, planar films, while few studies are available for cylindrical polymer nanowires. Properties of a cylindrically confined polymer may greatly differ from its properties in bulk state when the geometrical restrictions approach the size of the polymer itself. Confinement of polymer dielectrics in nanoporous templates can potentially enhance the dielectric properties of the material via directed crystallization. A study of the effects of directed crystallization will provide a new level of crystallization control for this group of polymers.

2. BACKGROUND

2.1: Confinement Effects – Block Copolymers

The physical properties of a semi-crystalline polymer confined to a small dimension greatly differ from its properties in the bulk state. A polymer is said to be "confined" when it is constricted in geometries smaller than its unperturbed molecular size.[3] Polymer dielectrics, such as isotactic poly(propylene) (iPP) and polycarbonate (PC) are of interest in this regard because confinement perhaps might be leveraged to control crystallization and, in turn, other physical properties. For example, iPP is used widely as the dielectric layer in capacitors,[4] as a packaging material for perishables,[5] and as a non-woven textile[6]; each of these applications relies on manipulating crystallinity to achieve a desired property (*e.g.* dielectric permittivity, permeability, or mechanical strength). To some extent, the length scale of confinement might be viewed as another tuning parameter for the crystallization of iPP and its resulting properties.

A wide variety of examples are available that highlight how a semi-crystalline polymer's thermal properties change due to confinement effects. Crystallization and morphology of diblock copolymers containing a crystallizing segment have been studied.[7-12] Loo *et al.* demonstrated that the crystallization of polyethylene (PE) within styrene-ethylene-butene random terpolymer blocks follows first order kinetics and is homogeneously nucleated, where the polymer phase separated into spherical microdomains of ~25 - 30 nm in diameter; in contrast, bulk PE generally follows

sigmoidal kinetics.[9, 10] PE crystallized within a poly(vinylcyclohexane) glassy matrix also showed first order kinetics and homogeneous nucleation when phase separated into spherical or cylindrical microdomains.[11] Elsewhere, poly(ethylene oxide)-*b*-polystyrene (PEO-*b*-PS) diblock copolymers have been observed to form lamellae structures within which the PEO block was confined to a thickness of ~ 8.8 nm.[12] PEO also varied its orientation with crystallization temperature[12] and lamellae thickness.[8] Furthermore, when the PEO-*b*-PS diblock copolymer is additionally blended with PS homopolymer the PEO blocks transform into nanolcylinders ~ 14 nm in diameter and change orientation as the crystallization temperature increases.[7, 12]

2.2: Confinement Effects – Cylindrical

Polymer melt-wetting of nanoporous templates is often used as a convenient method for studying the behavior of polymers crystallizing in confined geometries and can be viewed as an alternative to using diblock copolymers. Generally, a polymer film is cast and then melt-wetted into a nanoporous template at some temperature above the polymer's glass transition temperature (T_g) or melting temperature (T_m) with or without applied pressure. The fundamentals of this process are well described by Zhang *et. al.* and Steinhart *et. al.* where the length of the resulting nanostructure is dictated by the melt-wetting time, the diameter of the pore, the viscosity of the polymer melt, and the surface tension. The spreading coefficient *S*, given in terms of the interfacial tensions between the solid surface and the surrounding gas (γ_{SG}), the surface and the liquid /

molten material (γ_{SL}) and the liquid-gas surface tension (γ_{LG}) by equation 2 below, can be used to describe the wetting of a solid surface by a liquid or a melt.

$$S = \gamma_{SG} - \gamma_{SL} - \gamma_{LG} \quad (2)$$

A molten polymer will spontaneously spread and fully cover the inner walls of the nanopores to form nanotubes if *S* is positive or zero. Nanorods will form if *S* is negative and the polymer will fill the nanopores through capillary action.[13] Figure 1 shows polystyrene nanotubes (Figure 1-a) and nanorods (Figure 1-b) obtained using different experimental conditions.

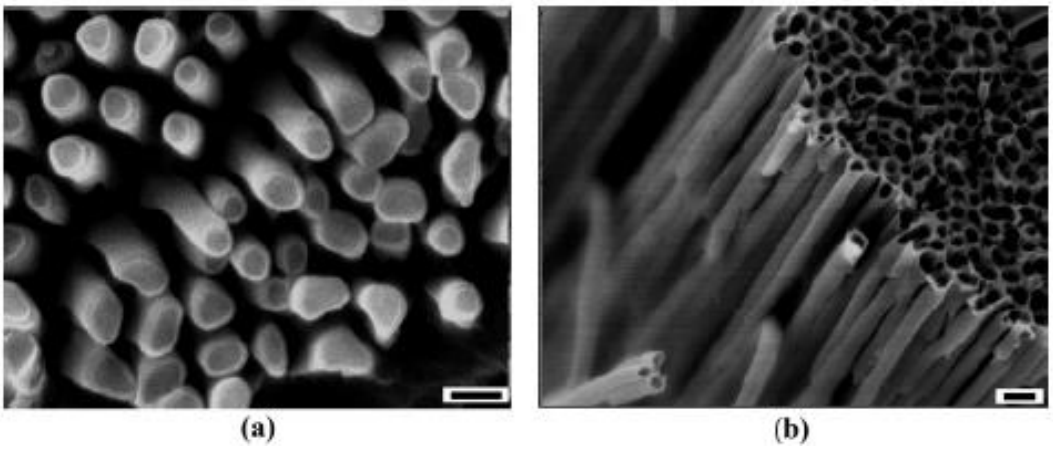

Figure 1. Polystyrene nanorods (a) and polystyrene nanotubes (b).[13] Reprinted with permission from Reference 13. Copyright 2006 American Chemical Society.

In the current study, anodic aluminum oxide (AAO) was chosen as a suitable nanoporous template due to its uniform pore length (~100 μm) and arrangement, as well as controllable pore diameter (15-200 nm) and monodispersity in size. Several previous

studies have shown successful wetting of nanoporous AAO templates with various polymers.[13-20]

Linear polyethylene was shown to nucleate heterogeneously when crystallized in AAO nanopores 15 – 48 nm in diameter and homogeneously in nanopores 62 nm in diameter or larger.[19] It was also shown that linear polyethylene oriented with the *b* – axis aligned parallel to the long axis of the nanopore when confined in nanopores 15 – 110 nm in diameter.[16] When confined in AAO nanopores 400 nm in diameter, poly(vinylidene difluoride) oriented with the *b* – axis aligned parallel to the long axis of the nanopore as seen with confined polyethylene.[17] Syndiotactic polystyrene, on the other hand, was shown to orient with the *c*-axis parallel to the long axis of the pore wall when crystallized from the molten state in AAO membranes.[20] Orientation of the ferroelectric β phase was demonstrated for poly(vinylidene fluoride-co-trifluoroethylene), and the melting and crystallization temperatures were also shown to decrease as the polymer was placed into more stringent confinement.[14, 15] These examples serve to show that cylindrical confinement can direct crystallization via curvature, which becomes increasingly important as the diameter of the pore decreases.

Here, we investigate relationships between crystallization and pore diameter for iPP melt-wetted into AAO templates bearing 15, 40, and 200 nm diameter pores (iPP-15, iPP-40, and iPP-200, respectively). For the first time, orientation of iPP crystallites within AAO pores is demonstrated using X-ray diffraction with texture analysis. Avrami crystallization kinetics analysis is used to demonstrate that the origin of this orientation

is related to the impingement of crystals against the pore wall, thus “freezing out” polymer crystallizing in non-preferred directions.

3. ISOTACTIC POLYPROPYLENE NANOWIRES

3.1: Formation of Isotactic Polypropylene Nanowires

Anodic aluminum oxide (AAO) templates were fabricated from aluminum foil (99.999 %, Sigma Aldrich) using a two-step electrochemical oxidation method.[21] Anodization of aluminum in 0.3 M sulfuric acid solution at 25 V or in 0.3 M oxalic acid solution at 40 V resulted in self-ordered pores of 15 or 40 nm diameter, respectively. Isotactic polypropylene (iPP) was purchased from Sigma Aldrich. The molecular weight and dispersity were determined to be M_w~243,000 g/mol and 2.18, respectively using gel permeation chromatography. Following recrystallization from p-xylene to remove any remaining catalyst and impurities, the molecular weight and dispersity were 241,000 g/mol and 2.19, respectively. To perform the recrystallization, the polymer was first brought to a boil in a ~1 wt% solution, and then allowed to cool to room temperature. The resulting solution was filtered using Whatman brand Grade 1 filter paper. The resulting powder was dried overnight under vacuum oven at 80 ^{o}C to remove residual solvent.

Differential scanning calorimetry scans of the sample before and after recrystallization reveal stark differences, Figure 2. Firstly, the exothermic peak maximum shifted from 125 ^{o}C to 111 ^{o}C following recrystallization; secondly, the asymmetric shoulder on the crystallization peak disappeared. Both changes were attributed to the removal of impurities from the as-purchased material.

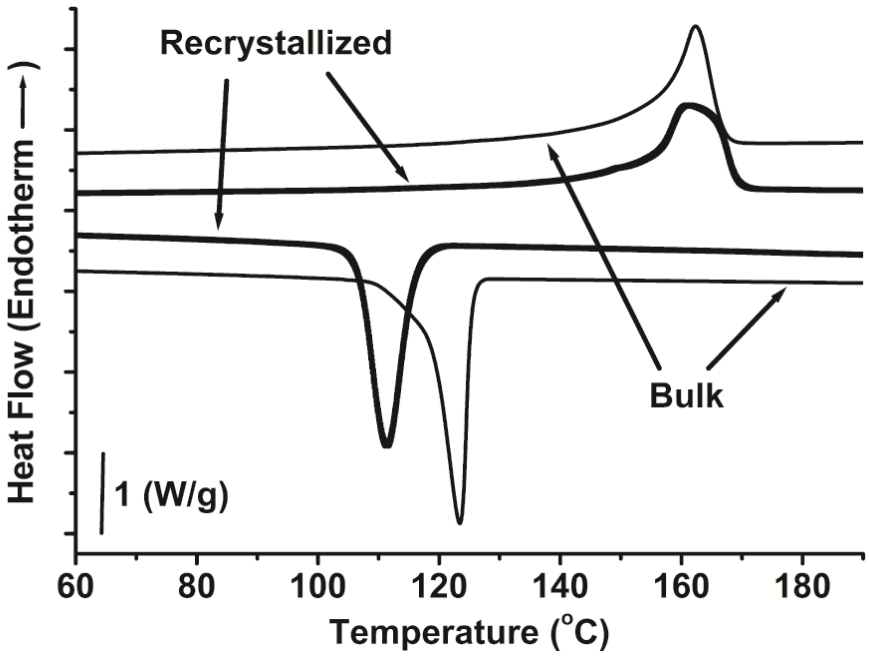

Figure 2. Heating and cooling thermograms of as-purchased and recrystallized iPP. Scan rate = 10 °C/min. Second scan shown.

Resultant iPP powder was hot pressed into sheets at 166 ^{o}C with a load of 4 metric tons for two sets of eight minutes. An AAO template was placed directly on top of an iPP sheet, sandwiched between two glass slides, and fastened with binder clips. Infiltration of iPP into the AAO template was conducted under vacuum at 200 ^{o}C for 20-24 hours. The samples were then immediately quenched on a steel plate. In order to prepare freestanding nanowires for scanning electron microscopy (SEM) imaging, the top glass slide was detached and the excess bulk polymer was mechanically removed with sandpaper. The top, un-infiltrated layer of alumina was etched away using a 5 wt% sodium hydroxide solution. Then the intermediate layer of aluminum was removed using a solution of copper (II) chloride in hydrochloric acid at a concentration of 0.05 g/ml.

The remaining alumina was then etched away using sodium hydroxide solution to release the nanostructures from the template.

Released nanowires were imaged using a JEOL JSM-7500F SEM. Figure 3 shows nanowires formed after melt-wetting and subsequent template removal. These results match well with Duran and co-workers, who have shown that nanorods form in AAO pores of 380 nm diameter under the same conditions.[22] The nanowires were largely uniform in diameter, and all were comparable in size to the template's pore diameters (200, 40, and 15 nm). Figure 3-d shows the top view an empty AAO template, where the pore diameter was ~ 40 nm. The pores were circular in shape, uniform in diameter, and organized in hexagonal arrays.

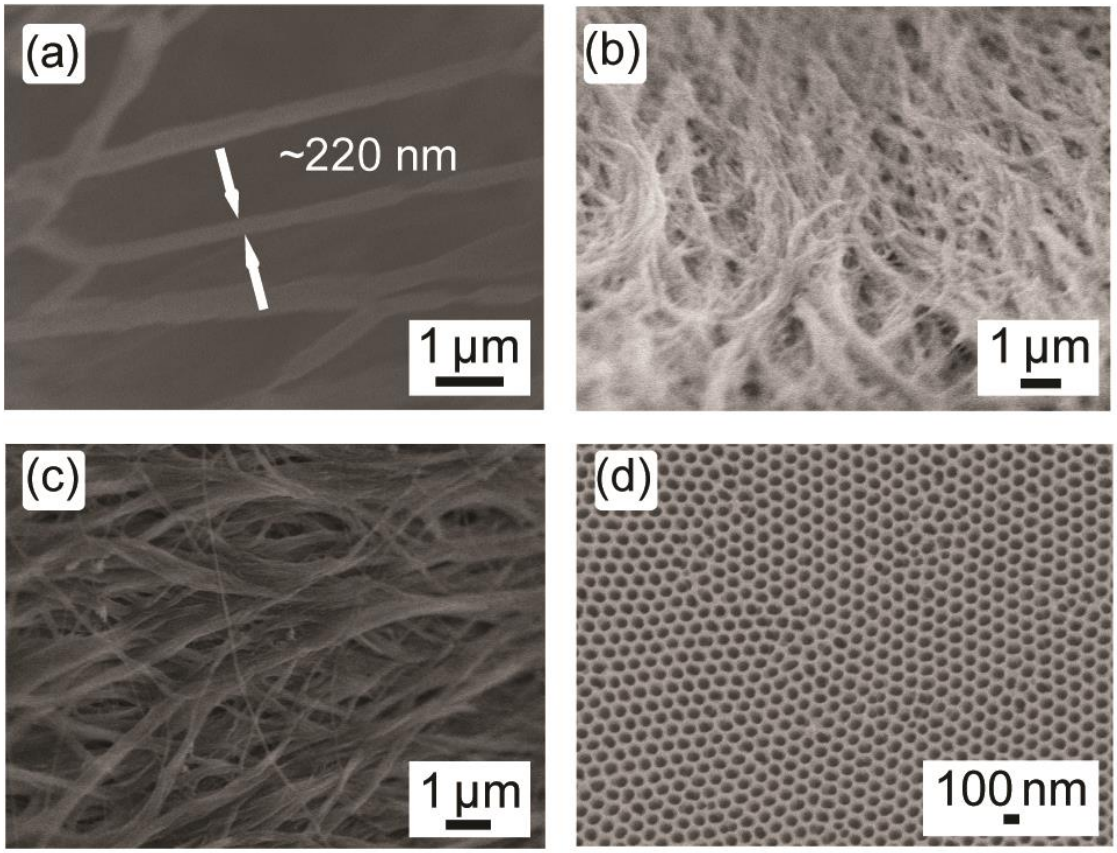

Figure 3. Scanning electron microscope (SEM) images of nanowires formed via melt-wetting of iPP into nanoporous AAO after template removal; structures derived from pore diameters of (a) 200 nm, (b) 40 nm, and (c) 15 nm are shown. (d) Top view of empty 40 nm pore diameter AAO templates.

3.2: Overall Crystallization Behavior of Confined iPP

The steps for preparation of confined iPP for differential scanning calorimetry (DSC) studies were as follows. The sample was placed in 5 wt% sodium hydroxide solution to remove the top alumina layer. A razor blade was then used to detach the sample from the bottom slide, and excess bulk polymer was removed using an O_2-

plasma etcher (Harrick Plasma PDC-32G). The etched surface was covered with Kapton tape and the sample was placed in a solution of copper (II) chloride as before. Thermal analysis was performed using a TA Instruments Q200 DSC. All DSC measurements were performed under a nitrogen atmosphere using Tzero aluminum pans and lids.

Figure 4 shows the effect of plasma etching on an AAO template (200 nm pore diameter) infiltrated with recrystallized iPP. The sample was exposed to 0, 1, or 2 hours of oxygen plasma, with the motivation of identifying the optimal etching duration. Without any etching, the untreated sample displayed a crystallization peak bearing a shoulder at slightly higher temperatures, Figure 4-b. After one hour of plasma treatment the excess bulk layer was successfully removed, and the confined polymer was exposed. This was confirmed by the appearance of a low-temperature crystallization peak in the cooling scan and the disappearance of the previously observed shoulder. After two hours of etching, the measured heat flow was greatly reduced, suggesting that the infiltrated polymer had been etched away. Therefore, one hour was selected as the optimal etching duration.

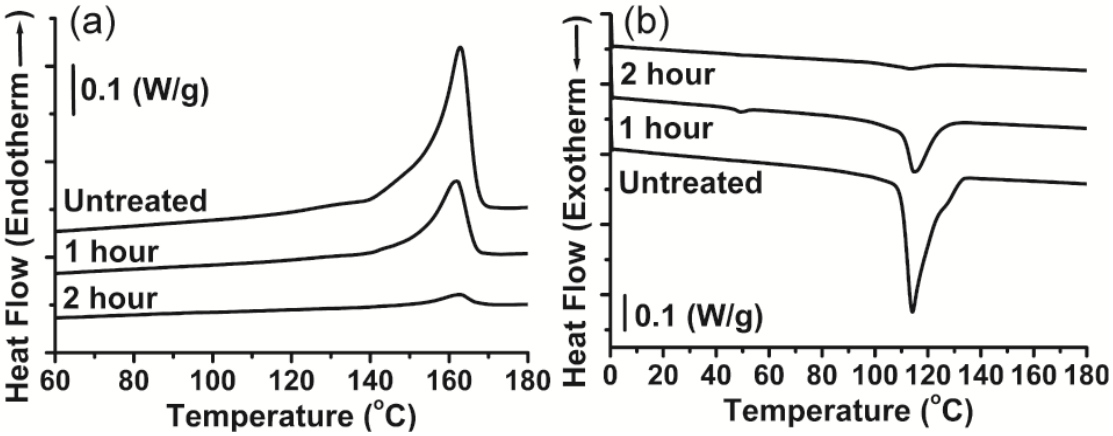

Figure 4. Heating (a) and cooling (b) thermograms of iPP infiltrated into an AAO template (200 nm pore diameter) exposed to varying durations of plasma treatment.

DSC was performed on bulk iPP and iPP confined in nanoporous AAO templates to identify the melting temperature, crystallization temperatures and heat of fusion as a function of pore diameter. DSC scans collected for empty AAO templates were featureless (not shown), whereas those imbibed with iPP showed distinct melting and crystallization features, Figure 5.

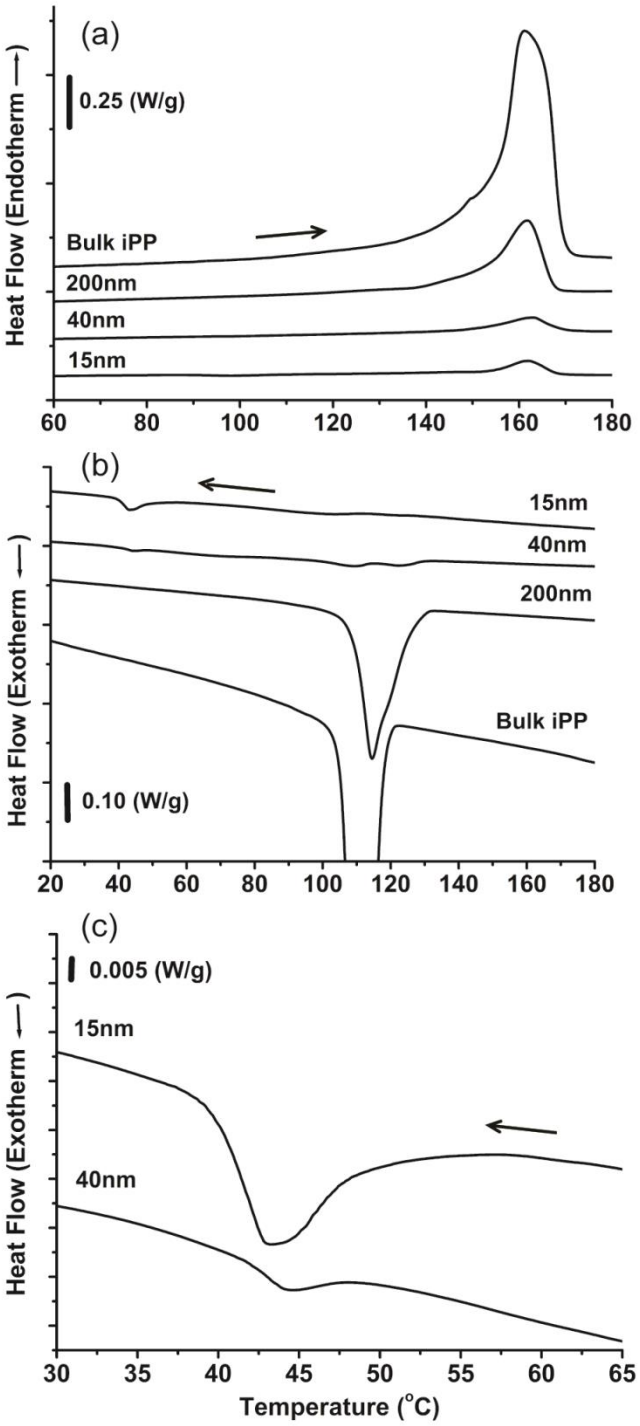

Figure 5. Heating (a) and cooling (b) DSC scans of bulk-iPP, iPP-200, iPP-40 and iPP-15; (c) an expanded view of the low-temperature exothermic peaks from (b). The scan rate was 10 ^{o}C/min.

The samples were heated and cooled at a rate of 10 ^{o}C/min. Upon heating a melting peak at about 162 ^{o}C was observed, the position of which was largely unaffected by pore diameter, Figure 5-a. However, as the pore dimensions decreased, the peak became weaker. Upon cooling, the bulk, 200 nm and 40 nm samples exhibited a crystallization peak at about ~109 ^{o}C, which became weaker and broader as the pore dimensions decreased, Figure 2b. The peak became fully undetectable in the 15 nm sample. Notably, other crystallization peaks appeared at 49.1 ^{o}C (iPP-200), 44.1 ^{o}C (iPP-40) and 43.4 ^{o}C (iPP-15), Figure 5-c. However, for iPP-200 out of a number of samples tested the homogeneous peak was only observed once. This occurrence could be due to incomplete removal of the surface polymer or additional incorporation of defects in larger sized pores. The shift to lower crystallization temperatures with decreasing diameter was also observed by Duran and co-workers but to a greater degree.[23] The lower temperature exothermic peak can be attributed to homogeneous nucleation while the high-temperature peak appears due to the formation of heterogeneous nuclei.[23] The calculated pore volume was ~ 3×10^{-9} mm^3, ~ 1×10^{-10} mm^3 and ~ 1×10^{-11} mm^3 for the 200 nm, 40 nm and 15 nm diameter templates, respectively. The volume of a single nucleus of iPP is ~5×10^{-7} mm^3 based on a reported spherulitic diameter of ~10 μm.[24] The pore volume of the 40 nm and 15 nm templates was significantly lower than that of a single nucleus thus, limiting the occurrence of defects from which heterogeneous nuclei form. For the 200 nm templates the volume difference was smaller allowing for a larger number of defects and a greater amount of heterogeneous nucleation.

Table 1 summarizes the thermal properties of the materials used. Polymer crystallization was initiated by either homogeneous, heterogeneous or self-nucleation, proceeded by crystal growth.[25]

Table 1. Thermal properties of confined iPP.

Samples	T_m (°C)	ΔH_f (J/g)[b]	T_h(°C)[a]	T_m^o (°C)
Bulk iPP	161.0 ± 0.2	104 ± 4	---	184.8 ± 0.4
iPP-200	161.7 ± 0.5	27 ± 9	49.1	175.2 ± 0.5
iPP-40	162.6 ± 0.3	6.5 ± 0.3	44.4 ± 0.2	172.9 ± 1.4
iPP-15	161.5 ± 1.1	5 ± 1	42.3 ± 0.9	163.1 ± 0.6

[a] Homogeneous crystallization temperature (T_h) taken from DSC cooling scans.
[b] Calculated using DSC heating scans.

3.3: Isothermal Crystallization Kinetics of Confined iPP

In order to determine the effect of pore diameter on the mechanism of crystallization for iPP in cylindrical nanopores, isothermal crystallization was performed using DSC for a series of temperatures. The samples were held at 200 °C for ten minutes to erase the thermal history. Then, the temperature was quickly dropped to the desired crystallization temperature and held isothermally for thirty minutes. This cycle was repeated for a range of crystallization temperatures. A schematic of the isothermal "recipe" is shown in Figure 6.

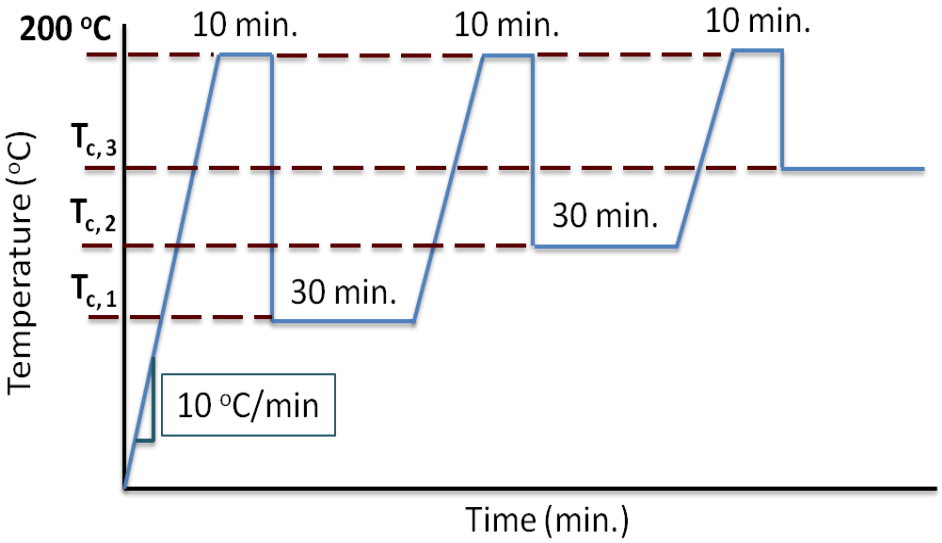

Figure 6. Schematic representation of the isothermal "recipe".

Figure 7 shows the crystallization isotherms for bulk-iPP, iPP-200 and iPP-40. Isothermal crystallization data for iPP-15 was not presented because no appreciable crystallization was detected for temperatures between 97 °C and 130 °C. Isothermal crystallization of bulk iPP was represented by a single peak, while isotherms for iPP-200 and iPP-40 were characterized by multiple overlapping peaks. Such behavior suggests that crystallization of iPP within the nanopores proceeds in multiple stages. Homogeneously nucleated crystals form at a site of chain aggregation; heterogeneously nucleated crystals form at foreign preexisting surfaces such as defects or impurities. Due to a reduction in surface energy, heterogeneous nucleation rates are faster than homogeneous.[25] As such, the features at early times in Figures 7-b and 7-c can be attributed to heterogeneous nucleation and those at longer times represent homogeneous nucleation. In comparison, bulk-iPP crystallizes mainly via heterogeneous nucleation.[26]

In all samples as crystallization temperature (T_c) increased the peak in heat flow shifted to longer times, signifying a decrease in the crystallization time.

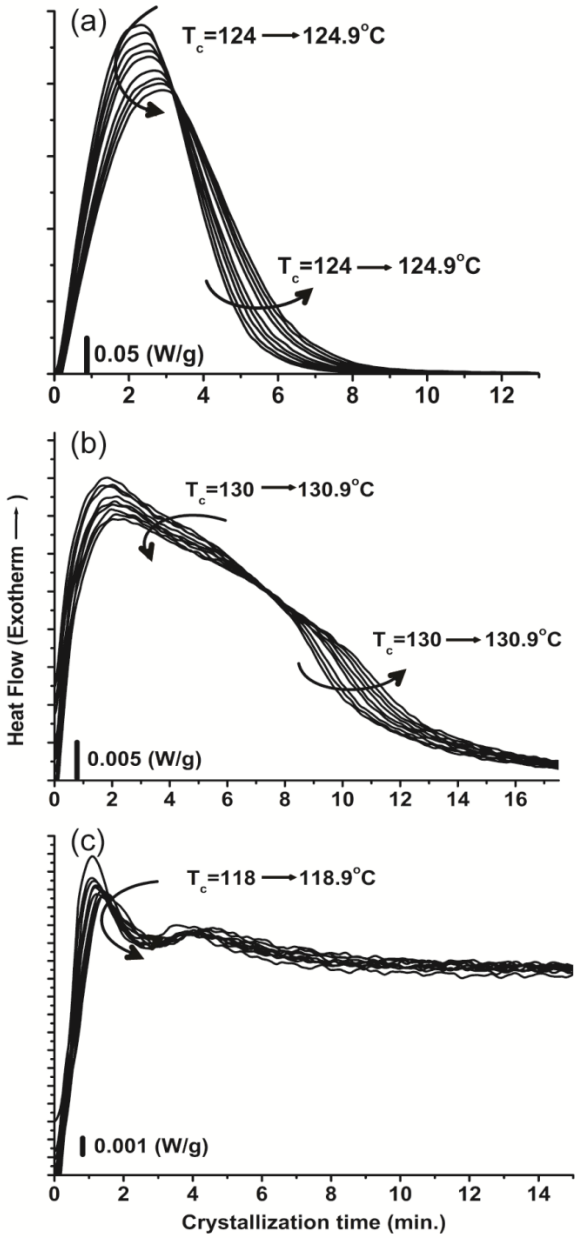

Figure 7. Heat flow as a function of time for isothermal crystallization of (a) bulk-iPP, (b) iPP-200, and (c) iPP-40.

To show the progression of crystallization with time and to obtain the crystalline fraction (*X)*, crystallization isotherms from Figure 7 were integrated using the following equation:

$$X(t) = \frac{\int_0^t \left(\frac{dH}{dt}\right) dt}{\int_0^\infty \left(\frac{dH}{dt}\right) dt} \quad (3)$$

where the numerator is the amount of heat evolved (*H*) at elapsed time *t* and the denominator is the total heat evolved during the course of crystallization, Figure 8. Bulk-iPP and iPP-200 show a sigmoidal shape characteristic of a nucleation and growth process.[25] However, iPP-40 deviates from sigmoidal behavior at longer times, suggesting a combination of nucleation and growth events.

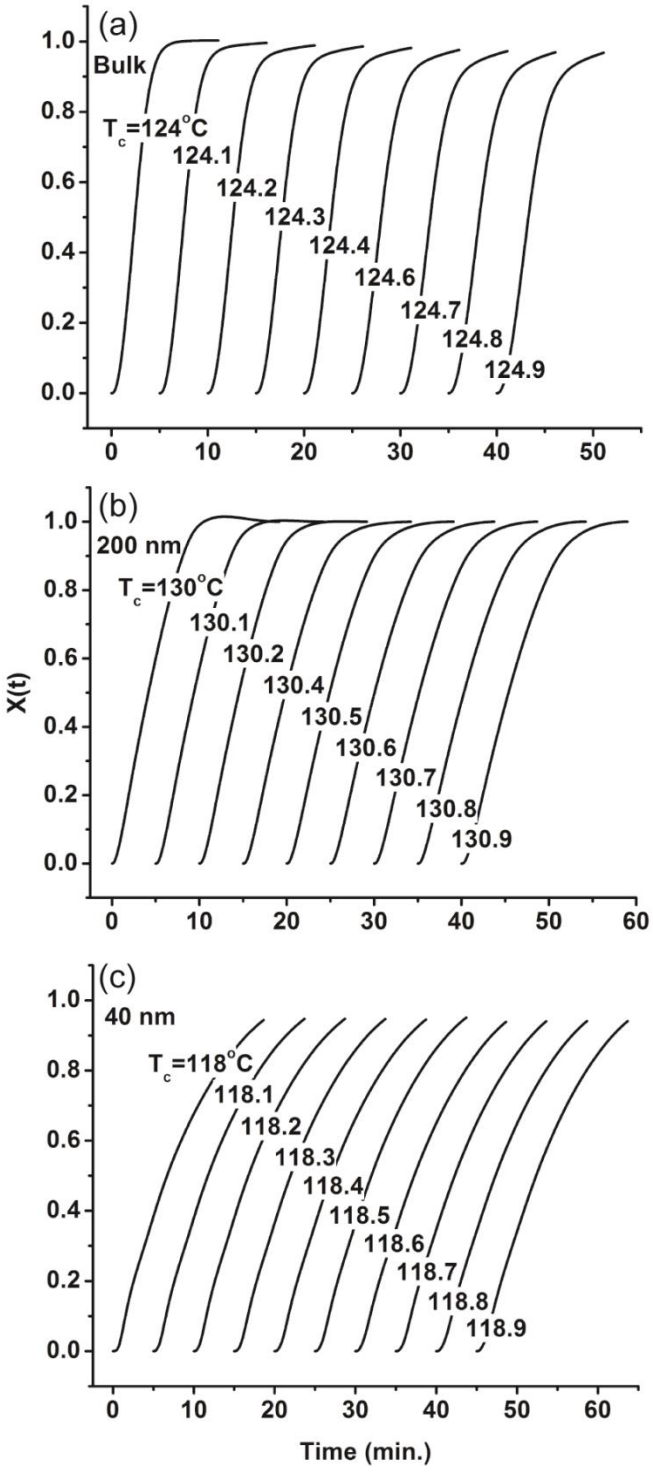

Figure 8. Crystalline mass fraction, X, as a function of time for (a) bulk-iPP, (b) iPP-200 and (c) iPP-40. Data were taken from Figure 7 and Equation 3.

The variation in the shape of the crystallization isotherms in Figures 7 and 8 suggests that pore diameter strongly influences how crystals form and grow. To understand the kinetics of crystal growth, Avrami analysis was applied according to the following equation:[27-29]

$$1 - \mathrm{X(t)} = \exp(-\mathrm{kt^n}) \qquad (4)$$

where *k* is the overall crystallization rate constant, *n* is the Avrami exponent, and *X(t)* is the crystalline mass fraction as a function of time. Theoretically the value of *n* should be an integer between 1 and 4, representative of the sum of the dimensionality (one, two, or three dimensions) the nucleation mode (zero for instantaneous and one for sporadic nucleation).[30] In practice, most values are non-integers due to two-stage crystal growth and/or mixed growth and nucleation modes.[25, 26] The Avrami equation can be rearranged into its linear form accordingly:

$$\log\left[-\ln\left(1 - X(t)\right)\right] = \log k + n\log t \qquad (5)$$

from which *n* and *k* can be obtained from the slope and the y-intercept, respectively. This analysis is good for time scales up to the impingement of spherulites ($X \approx 0.5$).[25, 30] Furthermore, the half-time of crystallization, $t_{1/2}$, can be collected from the plots of the crystalline mass fraction at X=0.5.

Figure 9 shows the resulting Avrami plots for the data shown in Figure 8. Following the recommendation posed by Lorenzo *et al*., Equation 5 was fit to regions where an acceptable coefficient of determination value could be obtained ($R^2 > 0.9990$), resulting in Table 2.[30] Both bulk and iPP-200 only required a single fit to achieve the

requisite R^2 value, resulting in a single set of n and k. However, a single fit was not possible for iPP-40; instead, three fits corresponding to three sets of n's and k's were required over different time scales of crystallization, discussed later.

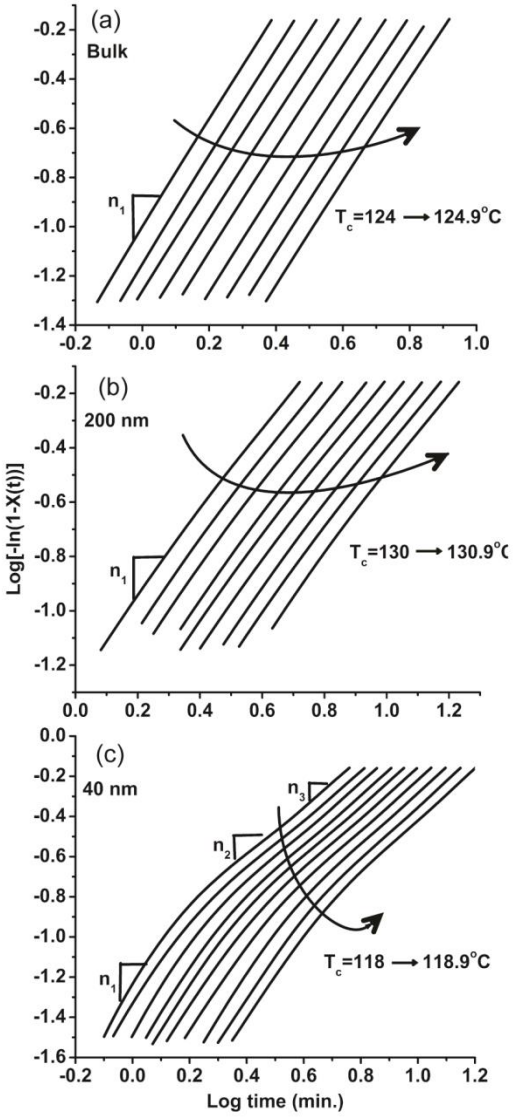

Figure 9. Avrami analysis of (a) bulk-iPP, (b) iPP-200 and (c) iPP-40 crystallized at various temperatures, T_c. The Avrami exponent, n, was calculated from linear fits of Equation 5 to the data.

Because bulk and iPP-200 were examined over similar ranges of crystallization their crystallization kinetics can be suitably compared. The Avrami exponent decreased from 2.11±0.04 in the bulk to 1.49±0.02 for iPP-200, signifying a decrease in the number of crystal dimensions. Considering that the iPP-200 DSC thermograms show a small amount of homogeneous nucleation, a shift from sporadic to instantaneous nucleation could also account for the decrease in *n*. In literature, the value of *n* for bulk iPP is most commonly 3.[31-33] However, some authors have reported values in the range of 2,[34-37] similar to our findings. Duran and coworkers reported values of *n* near 2 for iPP infiltrated into nanoporous AAO with a pore diameter of 380 nm, and values of *n* near 2.2 for iPP in 280 nm diameter pores.[19] The reduction of Avrami exponents has been previously reported for poly(ε-caprolactone)[38] and poly(ethylene oxide)[39] nanolayered films; as well as for polyethylene in AAO.[16, 19] Polyethylene was shown to have first-order kinetics when confined to microdomain blocks.[9-11] The crystallization rate for iPP-200 was ~1.2 times lower than that of bulk-iPP, Table 2. Decreases in *k* have also been reported for cyanurate trimer,[40] polyethylene[16, 19] and poly(ε-caprolactone)[38] under various forms of confinement. It can be observed that the half- time of crystallization ($t_{1/2}$) for iPP-200 was higher than for bulk iPP, due to restricted crystal growth. Increase in $t_{1/2}$ with imposed confinement has also been observed for cyanurate trimer in nanopores.[40] As well as, poly(ε-caprolactone) nanolayered films confined between layers of polystyrene and poly(methyl methacrylate).[38]

On the other hand, the crystallization kinetics for iPP-40 was quite different from that of iPP-200 and bulk iPP. The Avrami exponent decreased from 2.2 ± 0.2 at early

times to 1.24 ± 0.04, at later times. This behavior suggests that crystallization proceeds via two-dimensional growth with predominately heterogeneous nucleation initially; however, at longer times the exponent drops due to the crystallite growth becoming predominantly one-directional.[25]

Table 2. Avrami analysis for bulk iPP and iPP infiltrated into nanoporous AAO templates samples evaluated at various crystallization temperatures (T_c)

Samples	T_c (°C)	$t_{1/2}$ (min)[a]	Range	n	k (°C/min)	R^2
Bulk-iPP	124	2.43	0.048-0.499	2.185	0.100	0.9999
	124.1	2.53	0.049-0.497	2.179	0.091	0.9999
	124.2	2.63	0.049-0.499	2.108	0.090	0.9999
	124.3	2.73	0.050-0.500	2.107	0.084	0.9999
	124.4	2.83	0.052-0.504	2.099	0.079	0.9999
	124.6	3.00	0.050-0.500	2.095	0.070	0.9999
	124.7	3.10	0.050-0.498	2.086	0.066	0.9999
	124.8	3.10	0.052-0.478	2.082	0.062	0.9999
	124.9	3.30	0.049-0.502	2.081	0.059	0.9999
iPP-200	130	4.17	0.069-0.501	1.517	0.082	0.9990
	130.1	4.37	0.086-0.498	1.504	0.077	0.9990
	130.2	4.53	0.079-0.500	1.496	0.074	0.9990
	130.4	4.83	0.082-0.499	1.492	0.067	0.9990
	130.5	4.93	0.069-0.502	1.474	0.068	0.9990
	130.6	5.06	0.070-0.501	1.470	0.066	0.9990
	130.7	5.16	0.072-0.499	1.482	0.062	0.9990
	130.8	5.29	0.071-0.502	1.474	0.061	0.9990
	130.9	5.39	0.083-0.501	1.482	0.058	0.9990
iPP-40	118	5.13	0.031-0.055	2.644	0.080	0.9990
			0.110-0.149	1.601	0.082	0.9991
			0.153-0.501	1.184	0.099	0.9995

Table 2 continued.

T_c (°C)	$t_{1/2}$ (min)[a]	Range	n	k (°C/min)	R^2
		0.031-0.067	2.391	0.067	0.9991
118.2	5.33	0.086-0.131	1.726	0.070	0.9991
		0.134-0.499	1.230	0.088	0.9997
		0.031-0.087	2.194	0.063	0.9991
118.3	5.33	0.124-0.178	1.459	0.076	0.9990
		0.181-0.500	1.238	0.087	0.9997
		0.029-0.097	2.132	0.063	0,9990
118.4	5.38	0.119-0.182	1.455	0.075	0.9990
		0.185-0.500	1.238	0.086	0.9997
		0.030-0.100	2.057	0.063	0.9990
118.5	5.33	0.118-0.185	1.465	0.074	0.9991
		0.188-0.499	1.247	0.085	0.9998
		0.031-0.112	2.023	0.055	0.9991
118.6	5.55	0.125-0.203	1.416	0.071	0.9990
		0.206-0.501	1.261	0.079	0.9998
		0.030-0.096	2.170	0.051	0.9991
118.7	5.58	0.127-0.209	1.458	0.067	0.9991
		0.212-0.501	1.273	0.077	0.9999
		0.029-0.127	2.050	0.049	0.9991
118.8	5.61	0.137-0.241	1.389	0.068	0.9990
		0.244-0.500	1.296	0.074	0.9998
		0.030-0.120	2.020	0.050	0.9991
118.9	5.64	0.136-0.222	1.429	0.066	0.9990
		0.224-0.501	1.285	0.075	0.9998

[a] $t_{1/2}$ was taken as the time required to experimentally achieve $X(t)=0.5$, and was taken from Figure 8.

3.4: Equilibrium Melting Temperature

The equilibrium melting temperature (T_m^o) is a measure of the dimensions and perfection of a crystalline polymer, and can be experimentally determined using Hoffman-Weeks analysis.[41] The experimental melting temperature (T_m) is often lower than T_m^o due to surface effects and imperfections.[42] The experimental melting

temperature was obtained from DSC heating curves following isothermal crystallization at a series of temperatures. Initially, the sample was heated to 200 °C and held isothermally for ten minutes, to nullify the previous heating treatment. Next the sample was rapidly quenched to the desired crystallization temperature and held isothermally for thirty minutes. The melting temperature was collected by quenching the sample to 50 °C and heating it again above the melting temperature. The cycle was repeated for each crystallization temperature. A schematic of the steps outlined above is shown in Figure 10.

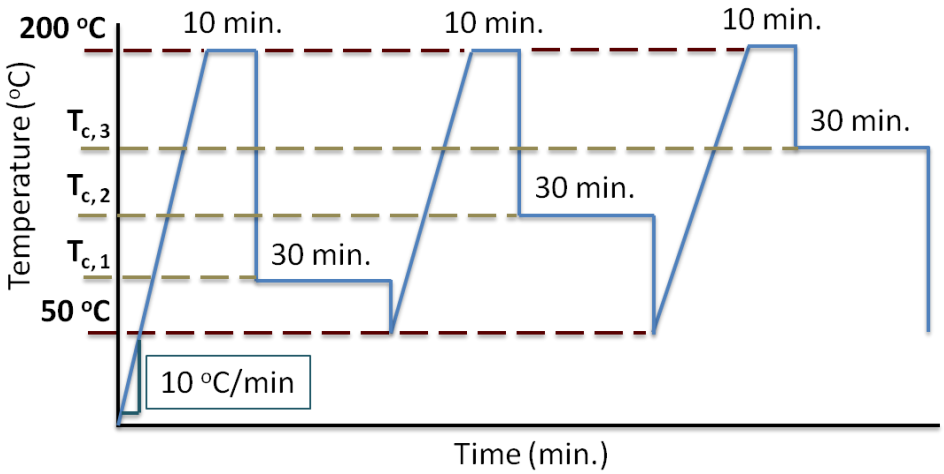

Figure 10. Schematic representation of the Hoffman-Weeks "recipe".

The resulting T_m values were plotted as a function of crystallization temperature (T_c), and T_m^o was obtained from the intersection of an extrapolated line with the diagonal T_m=T_c, Figure 11. The resultant T_m^o values were 184.8 $\pm$ 0.4 °C for bulk-iPP, 175.2 $\pm$ 0.5

^{o}C for iPP-200, 173$\pm$ 1 ^{o}C for iPP-40 and 163.1 $\pm$ 0.6 ^{o}C for iPP-15. Bulk-iPP's T_m^o was comparable to values reported in literature.[23, 26, 43, 44] This trend corroborates well with the Gibbs-Thomson equation[45] which predicts that the departure of the equilibrium melting temperature from that of the bulk is inversely related to diameter:

$$\Delta T_m^o = T_m^o(bulk) - T_m^o(d) = \frac{4\sigma_{sl}T_m^o(bulk)}{d\Delta H_f \rho_s} \quad (7)$$

where T_m^o is the equilibrium melting temperature, σ_{sl} is the solid–liquid interface energy, H_f is the bulk enthalpy of fusion of the material, ρ_s is the density of the material and d is the diameter of the confined dimension. As shown in Figure 11 the melting point depression does increase with decreasing pore diameter. For the given pore sizes, of 200 nm, 40 nm, and 15 nm, the ΔT_m^o is 9.6 $\pm$ 0.2 ^{o}C, 12$\pm$ 1 ^{o}C and 22 $\pm$ 1 ^{o}C, respectively.

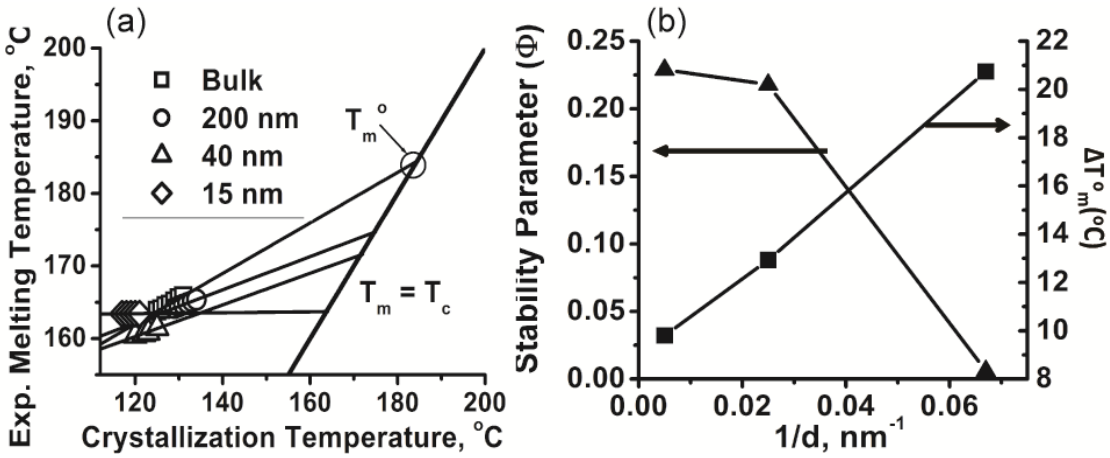

Figure 11. (a) Plot of experimental melting temperature as a function of crystallization temperature. (b) Stability parameter (Left Axis) and melting point depression (Right Axis) as a function of inverse nanopore diameter.

Additionally, T_m^o can be used to calculate the stability parameter Φ using the Hoffman-Weeks equation below:[42]

$$T_m^o - T_m = \Phi(T_m^o - T_c) \quad (8)$$

The stability parameter varies between one and zero and is a measure of the stability of a polymer crystal. As Φ approaches zero, T_m will approach T_m^o and the polymer will crystallize into its most stable form. Inversely, as Φ approaches unity T_m will approach T_c and the resulting polymer crystal will be unstable. From the values given in Figure 11, it can be observed that as the pore diameter decreases the perfection and stability of the crystalline polymer increases.

3.5: X-Ray Diffraction (XRD)

To prepare the samples for XRD analysis the sample was removed from the bottom slide using a razor blade and excess bulk polymer was mechanically removed using sand paper. θ/2θ diffraction patterns were collected in reflection mode (Bruker-AXS D8 Advance). The scanning increment and integration time were 0.03 ^{o} and 1 s, respectively.

From thermal analysis, it is suggested that crystallization is strongly affected by pore diameter. Therefore, X-ray diffraction was performed on bulk iPP, iPP-200, iPP-40 and iPP-15 to further understand crystal structure and orientation, Figure 12 and Table 3. Bragg-Brentano (θ-2θ) scans of iPP infiltrated into nanoporous AAO templates show an

overall reduction in peak intensity and sharpness relative to the bulk sample, Figure 12, which suggested a reduction in crystallinity with respect to reducing pore diameter. The peak reflections closely matched the values provided by ref #47 for the α-phase, which is the most common iPP polymorph.[46] The positions of the peaks for the infiltrated templates were largely comparable to that of the bulk sample; however some peaks had slight shifts in position but no clear trend with respect to pore diameter was observed. Also, peaks (130), (111) and (041) showed strong intensities in the bulk, but these reflections were not detected in iPP-200 and iPP-15. The (150) peak was not present for any of the confined samples.

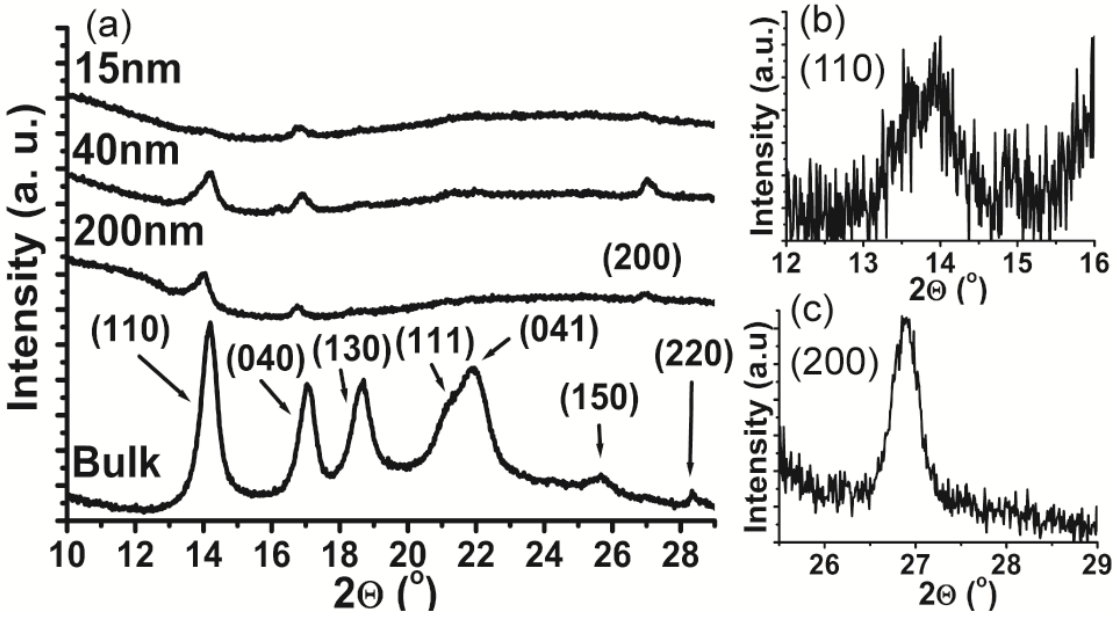

Figure 12. (a) θ/2θ patterns for bulk-iPP, iPP-200, iPP-40 and iPP-15. Magnified view of (b) (110) and (c) (200) peaks for iPP-15.

Table 3. 2θ values of (*hkl*) reflections for the α-phase of bulk iPP, iPP-200, iPP-40 and iPP-15. The 2θ diffraction angles are given for wavelength λ=0.154 nm.

$(h\ k\ l)_\alpha$	**2θ (°)**[47]	**d-spacing (nm)**	**2θ (°) Bulk-iPP**	**2θ (°) iPP-200**	**2θ (°) iPP-40**	**2θ (°) iPP-15**
(110)	14.14	0.626	14.18	14.06	14.24	13.98
(040)	16.92	0.524	17.07	16.77	16.90	16.71
(130)	18.55	0.478	18.70	---	18.56	---
(111)	21.31	0.417	21.12	---	21.37	---
(131)/(041)	21.86	0.406	21.99	---	21.94	---
(150)/(060)	25.35	0.351	25.66	---	---	---
(200)	27.18	0.328	---	27.04	27.02	26.94
(220)	28.51	0.313	28.33	---	---	---

3.6: Texture Analysis

Samples used for the X-Ray Diffraction studies with texture analysis were crystallized for an additional 30 minutes. The bulk sample was crystallized at 124.5 ^{o}C; the 200 nm, 40 nm and 15 nm samples were annealed at 130.5 ^{o}C, 118.5 ^{o}C and 116 ^{o}C, respectively. These values were chosen because they were similar to those used for Avrami analyses. The orientation of iPP infiltrated into AAO templates was investigated using a cradle. Tilt angle (Ψ) was varied from 0 ^{o} to 85 ^{o} in 1 ^{o} steps and with an integration time of 10 s. Data were collected by specifying the position of the incident and reflected beams, corresponding to a particular (*hkl*) plane, and collecting the intensities of the reflected rays as the sample stage was tilted by an angle Ψ. A schematic view of the experimental set-up for this analysis is shown in Fig. 13.

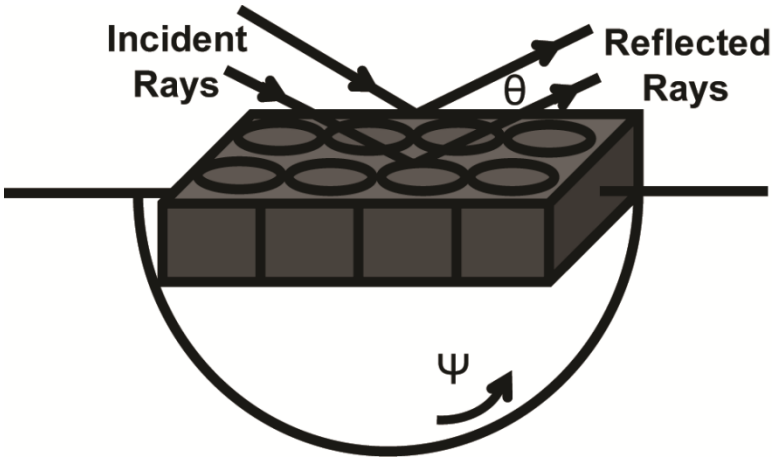

Figure 13. A representation of a polymer-infiltrated AAO template investigated using XRD. In this diagram, θ is fixed, and Ψ is allowed to vary.

Ψ-XRD patterns were collected to determine whether the polymer preferentially crystallizes relative to the direction of the pore wall, Figure 14. For iPP-200, only maximum intensities at Ψ=0 were detected. The lack of secondary Ψ-reflections indicated that crystallites formed in 200 nm-diameter pores possessed no discernible preference in orientation. For iPP-40 and iPP-15 samples the highest intensity occurred at Ψ=0 for {040} lattice planes. From this behavior, it was concluded that polymer chains preferentially oriented perpendicular to the long axis of the nanopore with the {040} planes arranged parallel to the surface of the sample. The second highest intensity at Ψ=0 corresponded to the {200} lattice planes, and corresponding reflections from interplanar angles were observed at Ψ=15 ^{o} and Ψ=44 ^{o} (iPP-40) and at Ψ=14 ^{o} and Ψ=43 ^{o} (iPP-15), which matched well with theoretical values of 17.5 ^{o} (200/110) and 43.3 ^{o} (200/130). This behavior led to the additional conclusion that iPP crystallites also displayed some preferential arrangement in the [200] direction, where {200} lattice

planes were also arranged perpendicular to the nanopore wall and parallel to the template surface.

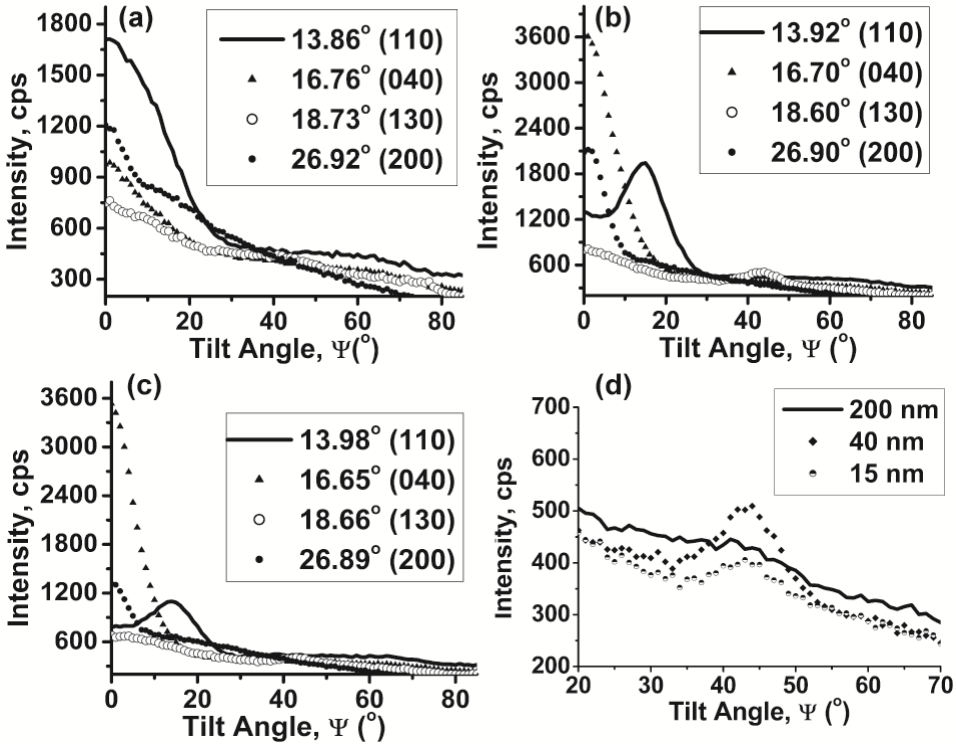

Figure 14. Ψ-XRD patterns of (a) iPP-200, (b) iPP-40 and (c) iPP-15 for various 2θ values.

Fig. 15 is a schematic representation of the proposed orientation of the polymer chains inside the 40 nm and 15 nm AAO nanopores. As the polymer is placed in stringent geometrical confinement the chains preferentially crystallize in the direction of the a- and b-axes. In other words, the polymer chains are oriented perpendicular to the

pore's axis. Similarly, the {040} and {200} family of planes are normal to the nanopore long axis and parallel to the template surface.

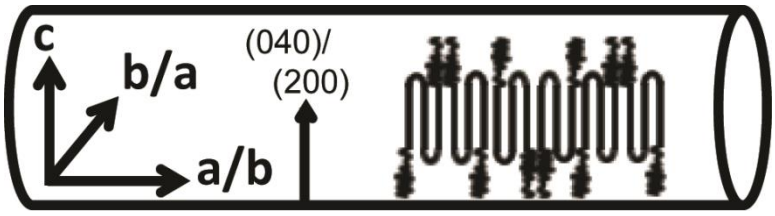

Figure 15. Schematic illustration of the iPP chain orientation relative to the long axis of the nanopore wall.

From the Avrami kinetics analysis and texture analysis presented previously, an origin for the 1-D orientation in pore diameters less than 40 nm as it relates the crystallization process can be proposed. Figure 16 illustrates the progression of crystallite growth with time. At the beginning of crystal growth, polymer chains are randomly oriented throughout the nanopore (top row). With time, as growth progresses, only chains oriented parallel to the nanopore wall continue to grow (middle row). All other chains are physically impinged by the nanopore walls (middle and bottom row). For polymer confined in the template bearing 200 nm diameter pores this effect does not occur due to the reduced surface area and decreased radius of curvature.

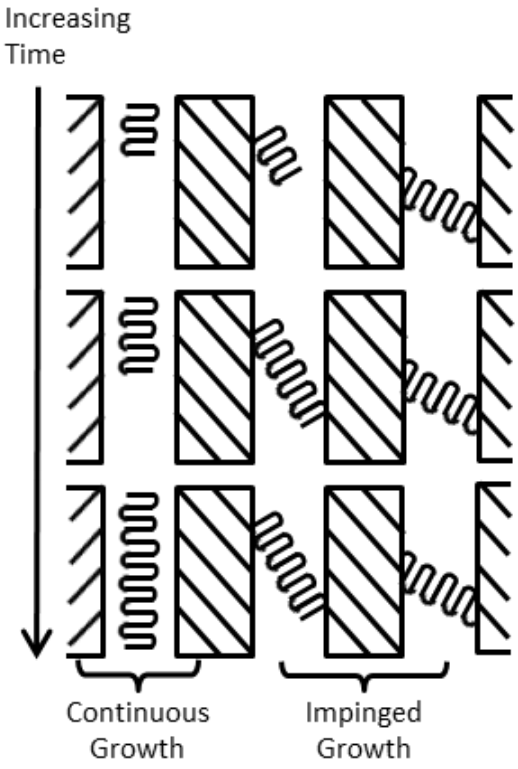

Figure 16. Schematic view of the orientation of the iPP crystallites formed inside AAO templates in relation to the pore wall.

4. POLYCARBONATE NANOWIRES

4.1: Introduction

Crystallization of polycarbonate (PC) is not as well documented as other polymers owing to its slow crystallization kinetics. As shown in Figure 17, with increasing polymer molecular weight the half time of crystallization is on the order of weeks. The data also shows that the maximum rate of crystallization occurs at 190 ^{o}C and is independent of the molecular weight.[48]

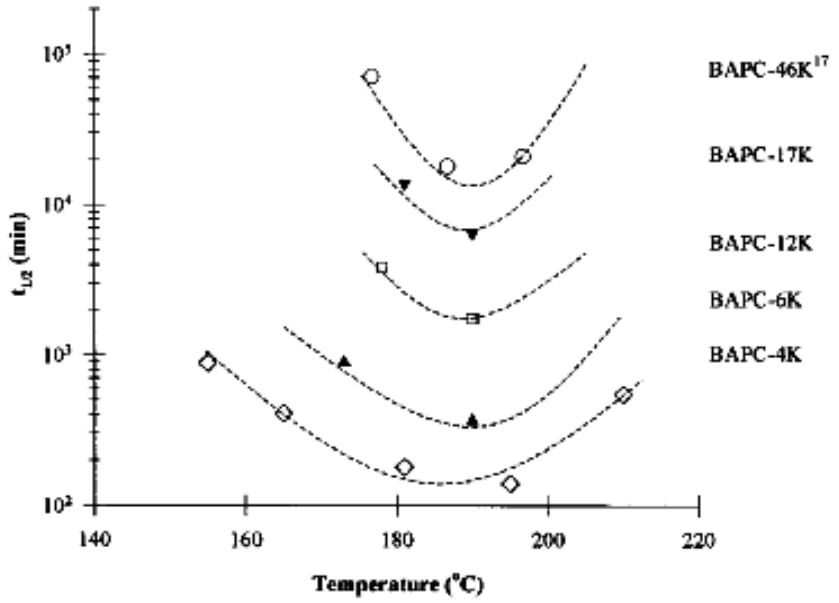

Figure 17. Half-time of crystallization of polycarbonate of various molecular weights as a function of crystallization temperature.[48] Reprinted with permission from Reference 48. Copyright 2001 American Chemical Society.

An additional challenge of working with polycarbonate is its high melting temperature (220 ^{o}C as reported by manufacturer). Previous thermogravimetric studies have shown that the polymer does not begin to degrade until ~300 ^{o}C both in the presence of nitrogen and air,[49] as shown in Figure 18.

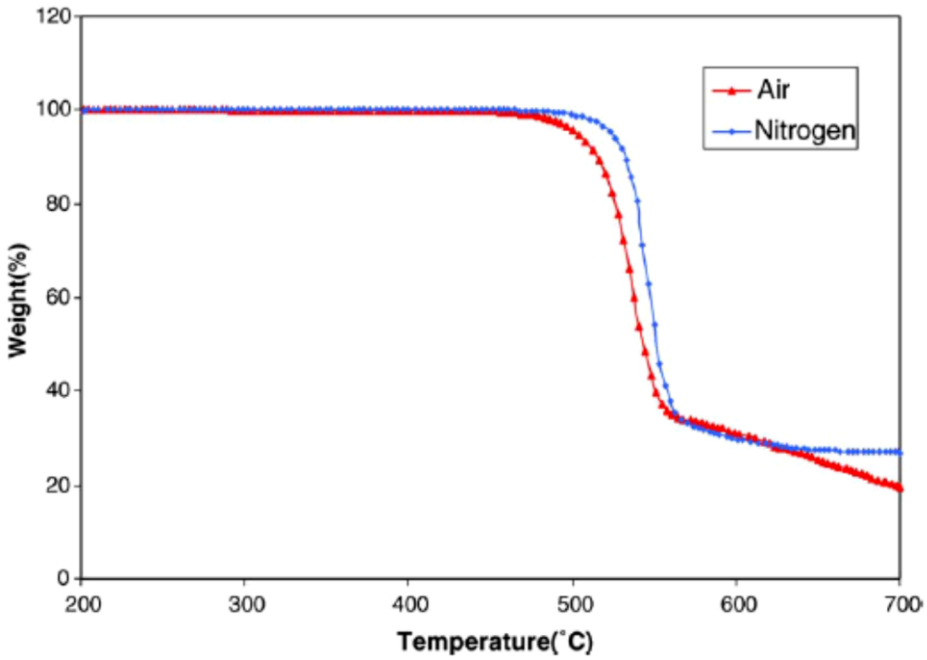

Figure 18. Thermogravimetric analysis curves for Bisphenol A Polycarbonate at a heating rate of 20 ^{o}C per minute in nitrogen and air.[49] Reprinted from Thermochimica Acta, 426 /1-2, Jang, B. N.; Wilkie, C. A., The thermal degradation of bisphenol A polycarbonate in air, 73-84, 2005, with permission from Elsevier.

However, other studies have shown that there is some oxygen uptake in PC when heated to 200 ^{o}C,[50] see Figure 19.

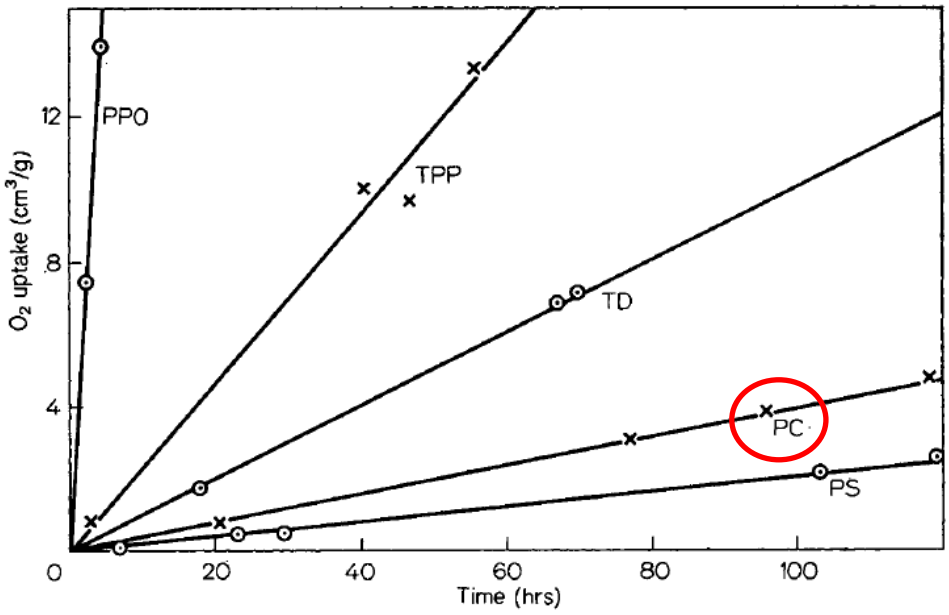

Figure 19. Oxygen uptake as a function of time for a range of aromatic polymers. Measurements collected at 200 °C.[50] Reprinted from Die Makromolekulare Chemie, 132 /1, Davis, A., Comparison of the thermal and thermo oxidative stability of polycarbonate, polyphenylene oxide, polysulphone and two polyarylates, 23-33, 1970, with permission from John Wiley and Sons.

4.2: Crystallized Bulk Polycarbonate

As purchased-PC was recrystallized from chloroform to remove any impurities. PC was dissolved in chloroform at a concentration of 5 wt%. The solution was heated at a low-rolling boiling for five minutes while stirring. Methanol was slowly added until small polymer flakes began to appear. The solution was then taken off heat and slowly cooled to room temperature. To achieve maximum precipitation of the product, the solution was cooled in a fridge overnight. The precipitated product was warmed to room temperature, filtered using Whatman brand Grade 1 filter paper and rinsed twice with

methanol. The resulting powder was vacuum dried overnight at 70 ^{o}C to remove residual solvent. Figure 20 shows the thermograms of the PC before (Figure 20-a) and after (Figure 20-b) the recrystallization. Both T_gs collected upon heating (145.95 ^{o}C for as-purchased and 151.36 ^{o}C for recrystallized) fall within a reasonable margin of error to the T_g reported by the manufacturer (148 ^{o}C).

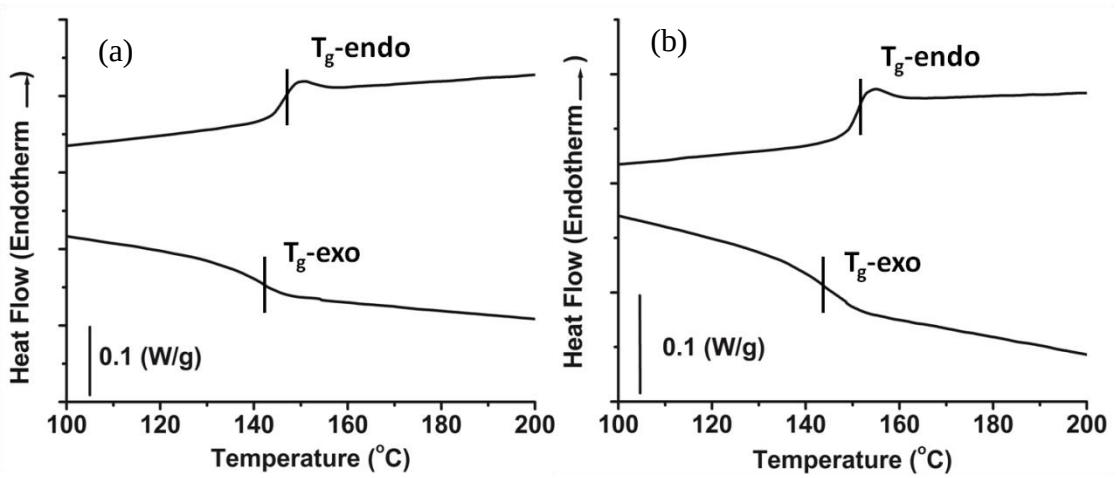

Figure 20. Heating and cooling thermograms of as-purchased (a) and recrystallized (b) PC. Scan rate = 10 °C/min. Second scan shown.

As shown in the thermograms above, the purchased-PC only displays a T_g and thus no significant amount of crystalline material was present. To induce crystallization, bulk material was heated under vacuum to 230 ^{o}C and held isothermally for thirty minutes to erase the thermal history. Then the temperature was reduced to 190 ^{o}C and annealed for 96 hours or four days. Figures 21-a and 21-b show thermograms of the first and second scans, respectively, of the crystallized PC. The first scan displays a low-

temperature melting peak at 219.9 ^{o}C +/- 0.3 ^{o}C and a shoulder at 237.6 ^{o}C +/- 0.3 ^{o}C. The second scan shows a T_g upon heating at 151.6 ^{o}C +/- 0.1 ^{o}C and a T_g upon cooling at 147.2 ^{o}C +/- 0.2 ^{o}C.

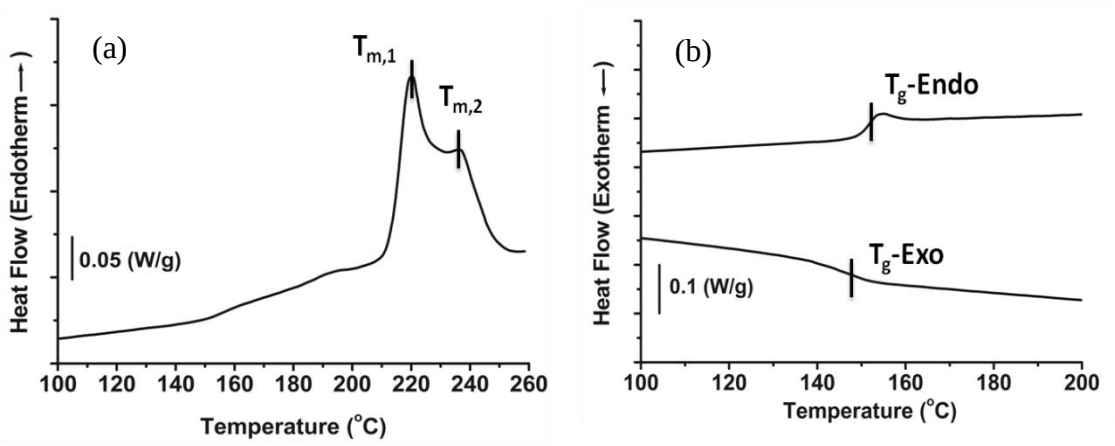

Figure 21. Heating and cooling thermograms of crystallized PC for first scan (a) and (b) second scan. Scan rate = 10 °C/min.

4.3: Polycarbonate 200 nm Nanowire Formation

Due to the extremely slow crystallization rate of polycarbonate, the prior techniques used in the formation of iPP nanowires are inadequate. Initial attempts to melt-wet the polymer using a vacuum oven yielded nanorods of insufficient length. To prepare the nanorods, PC was hot pressed into a sheet at ~ 232 ^{o}C and four metric tons for ~ 10 minutes. The polymer sheet was then placed on top of a 200 nm template, sandwiched between two glass slides and heated in vacuum oven at 230 ^{o}C. Figure 22-a

shows the resultant nanorods after 24 hours of heating and Figure 22-b after 55 hours. By comparing the two images it was observed that the length of the nanorods did not significantly increase. Thus, to keep the procedure within reasonable time limits a different method needed to be devised.

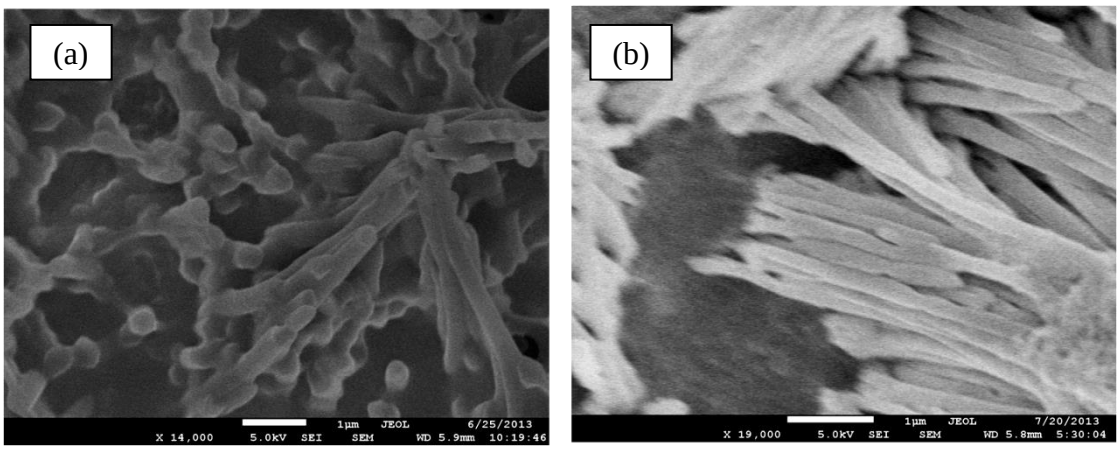

Figure 22. Polycarbonate nanorods after 24 hours (a) and 55 hours (b) of annealing.

In order to enhance the infiltration of the polymer into the nanopore, pressure was applied. A series of procedures was tested to determine the method, which would yield solid-core nanowires rather than hollow nanotubes. All samples were hot-pressed at ~232 ^{o}C and 0.25 metric tons of pressure for three hours. However, the preparation of the preliminary bulk film varied. To prepare the freestanding nanostructures to be viewed under the SEM, the samples were etched in 5 wt% solution of sodium hydroxide. Figure 23-a shows nanostructures formed using a film, which had been hot-pressed from bulk PC as described previously for the vacuum oven samples. Nanostructures shown in

Figure 23-b resulted from drop-casting ten drops of a 10 wt% solution of PC in chloroform directly onto a 200 nm template then drying. The process is termed solution-wetting. In Figure 23-a, the nanostructures display a meniscus, which is indicative of nanowire formation, but the exact form the polymer has adopted is unclear from the images in Figures 23-a and 23-b. Structures shown in Figures 23-c and 23-d display a definitively solid core. The nanowires were formed using a bulk polymer film, which has been drop-cast from a 10 wt% solution of PC in chloroform and dried overnight. Additionally, to prepare the sample shown in Figure 23-d the sodium hydroxide etching time was reduced to five minutes in order to reveal the partially etched polymer-filled AAO surface.

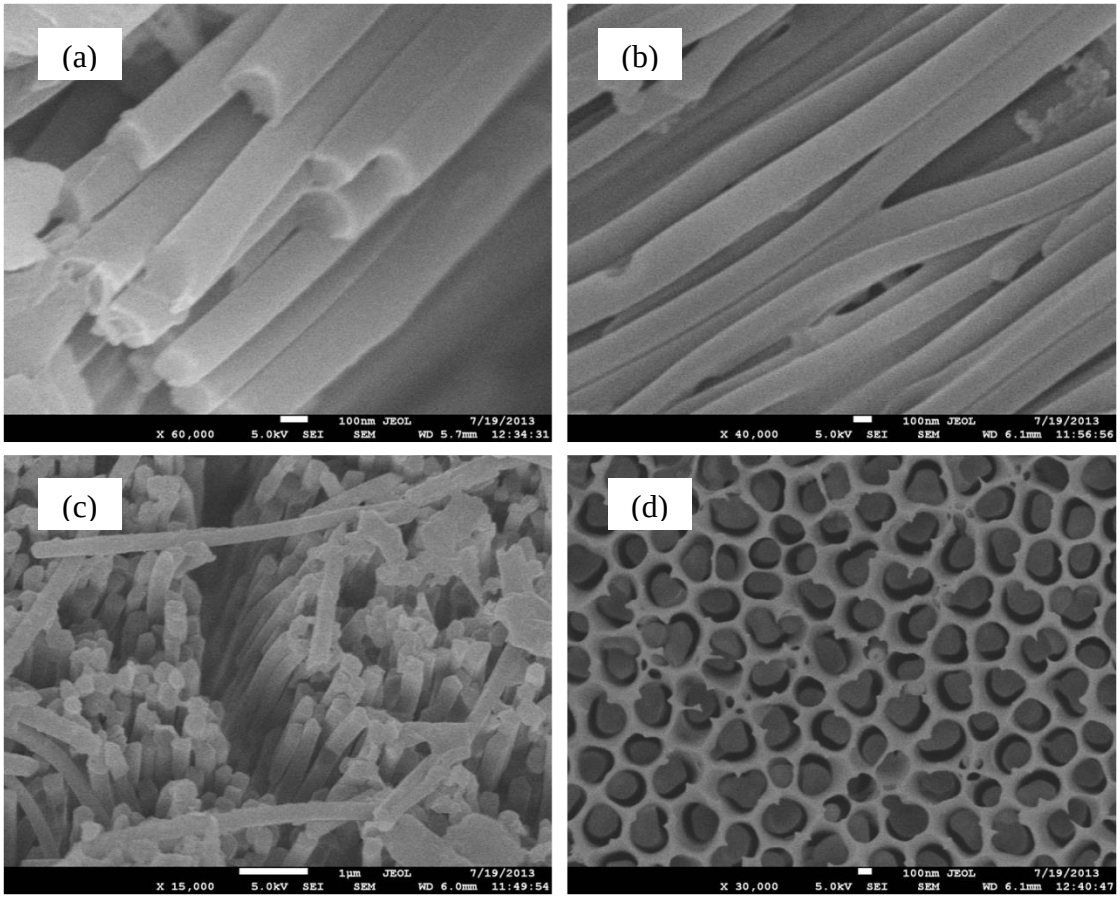

Figure 23. PC nanostructures formed using a hot-pressed PC film (a), solution-wetting (b) and a drop cast PC film (c).

4.4: Polycarbonate 200 nm Nanowires – Thermal Properties

To investigate the crystallization of PC within the confines of AAO nanopores the polymer nanowires were crystallized under vacuum for 96 hours, or four days, at 190 ^{o}C then quenched on a steel plate to preserve the crystalline structure. Prior to annealing, the samples were heated at 230 ^{o}C under vacuum for thirty minute to erase the thermal history caused by the hot-pressing procedure. The resultant crystallized samples were

prepared for DSC studies as described earlier in Chapter 3.2. The endotherm, presented in Figure 24, shows a single melting peak with a maximum at 226.0 ^{o}C +/- 0.5 ^{o}C. The second scans and higher were featureless and did not display a glass transition as seen in the crystallized bulk samples. Further studies are necessary to establish any pattern in the changes of the melting behavior of bulk PC and PC confined to AAO nanopores.

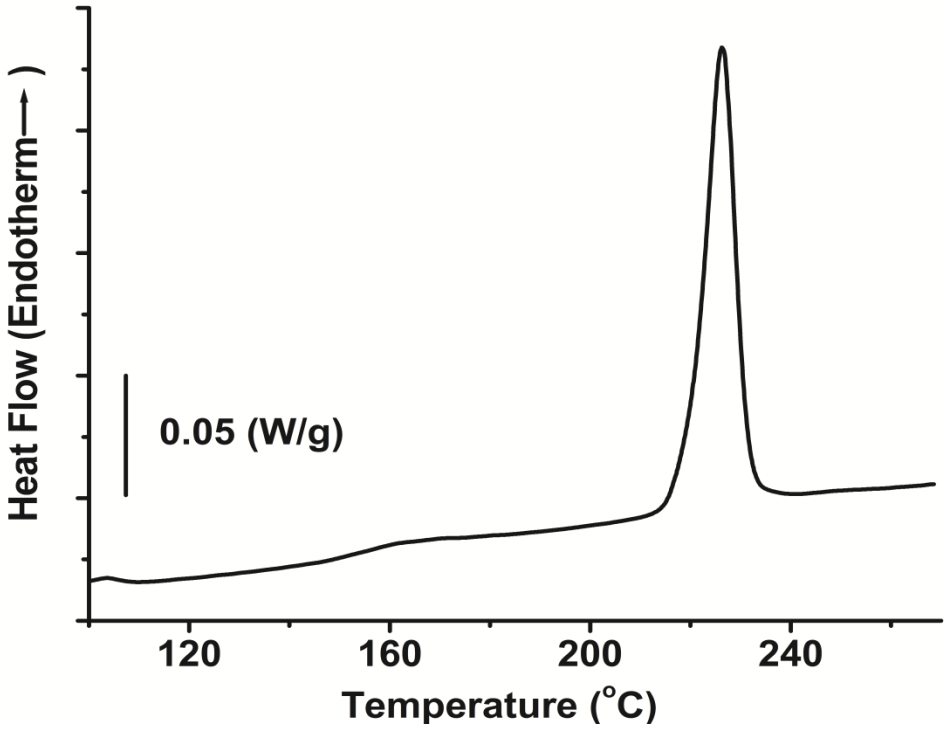

Figure 24. Endothermic scan of crystallized PC confined in 200 nm AAO. Scan rate = 10 °C/min. First scan shown.

5. BROADBAND DIELECTRIC SPECTROSCOPY

5.1: Introduction to Broadband Dielectric Spectroscopy of iPP-Filled AAO Templates

Broadband dielectric spectroscopy (BDS) is a tool to measure the dynamics of polymeric systems. Data is collected by applying an electric field and measuring the polarization of the sample. Features at various frequency ranges can be attributed to different relaxation and polarization processes.[51] The overall capacitance (C) can be determined using the collected data and the dielectric constant of iPP (ε_{iPP}) can be calculated using the following equation:

$$C_{tot} = \frac{\varepsilon_r \varepsilon_o A_{tot}}{l} = \frac{\varepsilon_{AAO} \varepsilon_o ((1-\varphi)A_{tot})}{l} + \frac{\varepsilon_{iPP} \varepsilon_o \varphi A_{tot}}{l} \qquad (9)$$

Where l is the pore length, φ is the porosity of AAO, A_{tot} is total area of the device and ε and ε_{AAO} are the dielectric constants of free-space and AAO, respectively.[52] However in practice, equation 9 is difficult to use because the necessary constants are not readily available and certain assumptions must be made. Figure 25 is a schematic representation of the tested samples where the applied field encounters AAO and iPP in parallel. Additional challenges arise due to the presence of an insulating AAO barrier layer which has been previously reported to be on average 10-100 nm thick.[53] Methods to remove this layer generally result in widening of the nanopores, which is undesired.

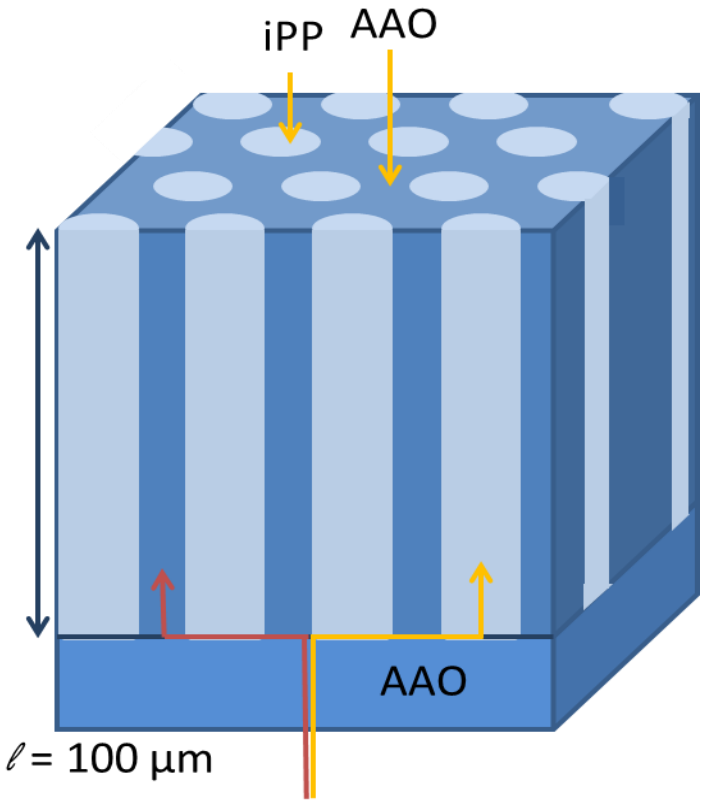

Figure 25. Schematic of confined iPP.

Additional challenges arise due to the presence of an insulating AAO barrier layer which has been previously reported to be on average 10-100 nm thick.[53] Methods to remove this layer generally result in widening of the nanopores, which is undesired.

5.2: Sample BDS data of iPP-Filled AAO Templates

Figure 26 shows the dielectric constant, *E'*, of bulk iPP as a function of temperature for a number of frequencies. As reported in literature, the dielectric constant

of biaxially oriented polypropylene is 2.2,[4] which closely matches the range of values shown in Figure 26. The sudden increase at higher temperatures is due to the melting of the polymer and the resultant change in sample dimensions.

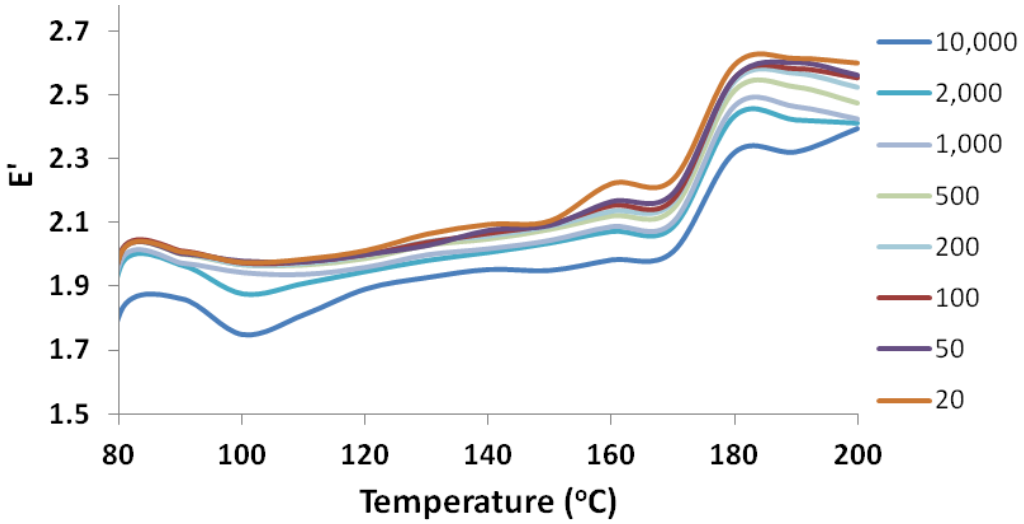

Figure 26. Dielectric constant as a function of temperature for a set of frequencies in units of Hz.

6. CONCLUSIONS

The effect of pore dimensions on the crystallization and orientation of iPP melt-wetted into nanoporous templates of varying diameter (15 – 200 nm) was investigated. It was shown that iPP crystallizes into the α-phase and preferentially orients along the long axis of the pore. A transition from hetero- to homogeneous crystallization was observed in relation to pore diameter. The isothermal crystallization kinetics was analyzed using Avrami analysis. It was observed that as the pore diameter decreases crystallization shifts to a multi-mode process, which originates in the alteration of the nucleation process and growth dimensions.

Crystallization of PC inside nanoporous AAO has proven to be a more difficult task due to the slow crystallization kinetics of the material. PC nanowires, 200 nm in diameter, were successfully fabricated and crystallized. Further changes need to be made to the fabrication procedure to generate nanowires 100 nm and 40 nm in diameter. Additionally, XRD studies are still needed to investigate whether polymer chain alignment within the confines of the nanopores.

Broadband dielectric studies have been a challenge due to the composite nature of the material tested. Further collection of dielectric constant and loss data would require reworking the sample preparation method.

REFERENCES

1. Tipler, P. A.; Mosca, G., *Physics for Scientists and Engineers*. Macmillan New York: 2007.
2. Hanemann, T.; Gesswein, H.; Schumacher, B. Dielectric Property Improvement of Polymer-Nanosized Strontium Titanate-Composites for Applications in Microelectronics. *Microsystem Technologies* **2011**, *17*, 1529-1535.
3. Forrest, J. A.; Dalnoki-Veress, K. The Glass Transition in Thin Polymer Films. *Advances in Colloid and Interface Science* **2001**, *94*, 167-195.
4. Rabuffi, M.; Picci, G. Status Quo and Future Prospects for Metallized Polypropylene Energy Storage Capacitors. *IEEE Trans. Plasma Sci.* **2002**, *30*, 1939-1942.
5. Isaka, T.; Matsuo, M.; Miyazaki, Y., Heat Sealable Laminated Propylene Polymer Packaging Material. Google Patents: 1980.
6. Pajgrt, O.; Reichstädter, B.; Ševčík, F., *Production and Applications of Polypropylene Textiles*. Elsevier New York: 1983.
7. Huang, P.; Zhu, L.; Cheng, S. Z. D.; Ge, Q.; Quirk, R. P.; Thomas, E. L.; Lotz, B.; Hsiao, B. S.; Liu, L. Z.; Yeh, F. J. Crystal Orientation Changes in Two-Dimensionally Confined Nanocylinders in a Poly(Ethylene Oxide)-B-Polystyrene/Polystyrene Blend. *Macromolecules* **2001**, *34*, 6649-6657.
8. Huang, P.; Zhu, L.; Guo, Y.; Ge, Q.; Jing, A. J.; Chen, W. Y.; Quirk, R. P.; Cheng, S. Z. D.; Thomas, E. L.; Lotz, B.*, et al.* Confinement Size Effect on

Crystal Orientation Changes of Poly(Ethylene Oxide) Blocks in Poly(Ethylene Oxide)-B-Polystyrene Diblock Copolymers. *Macromolecules* **2004**, *37*, 3689-3698.

9. Loo, Y. L.; Register, R. A.; Ryan, A. J. Polymer Crystallization in 25-Nm Spheres. *Phys. Rev. Lett.* **2000**, *84*, 4120-4123.

10. Loo, Y. L.; Register, R. A.; Ryan, A. J. Modes of Crystallization in Block Copolymer Microdomains: Breakout, Templated, and Confined. *Macromolecules* **2002**, *35*, 2365-2374.

11. Loo, Y. L.; Register, R. A.; Ryan, A. J.; Dee, G. T. Polymer Crystallization Confined in One, Two, or Three Dimensions. *Macromolecules* **2001**, *34*, 8968-8977.

12. Zhu, L.; Cheng, S. Z. D.; Calhoun, B. H.; Ge, Q.; Quirk, R. P.; Thomas, E. L.; Hsiao, B. S.; Yeh, F. J.; Lotz, B. Crystallization Temperature-Dependent Crystal Orientations within Nanoscale Confined Lamellae of a Self-Assembled Crystalline-Amorphous Diblock Copolymer. *J. Am. Chem. Soc.* **2000**, *122*, 5957-5967.

13. Zhang, M. F.; Dobriyal, P.; Chen, J. T.; Russell, T. P.; Olmo, J.; Merry, A. Wetting Transition in Cylindrical Alumina Nanopores with Polymer Melts. *Nano Lett.* **2006**, *6*, 1075-1079.

14. Lutkenhaus, J. L.; McEnnis, K.; Serghei, A.; Russell, T. P. Confinement Effects on Crystallization and Curie Transitions of Poly(Vinylidene Fluoride-Co-Trifluoroethylene). *Macromolecules* **2010**, *43*, 3844-3850.

15. Serghei, A.; Lutkenhaus, J. L.; Miranda, D. F.; McEnnis, K.; Kremer, F.; Russell, T. P. Density Fluctuations and Phase Transitions of Ferroelectric Polymer Nanowires. *Small* **2010**, *6*, 1822-1826.

16. Shin, K.; Woo, E.; Jeong, Y. G.; Kim, C.; Huh, J.; Kim, K. W. Crystalline Structures, Melting, and Crystallization of Linear Polyethylene in Cylindrical Nanopores. *Macromolecules* **2007**, *40*, 6617-6623.

17. Steinhart, M.; Senz, S.; Wehrspohn, R. B.; Gosele, U.; Wendorff, J. H. Curvature-Directed Crystallization of Poly(Vinylidene Difluoride) in Nanotube Walls. *Macromolecules* **2003**, *36*, 3646-3651.

18. Steinhart, M.; Wendorff, J. H.; Greiner, A.; Wehrspohn, R. B.; Nielsch, K.; Schilling, J.; Choi, J.; Gosele, U. Polymer Nanotubes by Wetting of Ordered Porous Templates. *Science* **2002**, *296*, 1997-1997.

19. Woo, E.; Huh, J.; Jeong, Y. G.; Shin, K. From Homogeneous to Heterogeneous Nucleation of Chain Molecules under Nanoscopic Cylindrical Confinement. *Phys. Rev. Lett.* **2007**, *98*.

20. Wu, H.; Wang, W.; Yang, H.; Su, Z. Crystallization and Orientation of Syndiotactic Polystyrene in Nanorods. *Macromolecules* **2007**, *40*, 4244-4249.

21. Masuda, H.; Fukuda, K. Ordered Metal Nanohole Arrays Made by a 2-Step Replication of Honeycomb Structures of Anodic Alumina. *Science* **1995**, *268*, 1466-1468.

22. Forrest, J. A.; Dalnoki-Veress, K. The Glass Transition in Thin Polymer Films. *Adv. Colloid Interface Sci.* **2001**, *94*, 167-196.

23. Duran, H.; Steinhart, M.; Butt, H. J.; Floudas, G. From Heterogeneous to Homogeneous Nucleation of Isotactic Poly(Propylene) Confined to Nanoporous Alumina. *Nano Lett.* **2011**, *11*, 1671-1675.

24. Coccorullo, I.; Pantani, R.; Titomanlio, G. Crystallization Kinetics and Solidified Structure in Ipp under High Cooling Rates. *Polymer* **2003**, *44*, 307-318.

25. Wunderlich, B., *Macromolecular Physics: Crystal Nucleation, Growth, Annealing*. Academic Press New York: 1976.

26. Chen, J. H.; Yao, B. X.; Su, W. B.; Yang, Y. B. Isothermal Crystallization Behavior of Isotactic Polypropylene Blended with Small Loading of Polyhedral Oligomeric Silsesquioxane. *Polymer* **2007**, *48*, 1756-1769.

27. Avrami, M. Kinetics of Phase Change I - General Theory. *J. Chem. Phys.* **1939**, *7*, 1103-1112.

28. Avrami, M. Granulation, Phase Change, and Microstructure - Kinetics of Phase Change. Iii. *J. Chem. Phys.* **1941**, *9*, 177-184.

29. Avrami, M. Kinetics of Phase Change. Ii Transformation-Time Relations for Random Distribution of Nuclei. *J. Chem. Phys.* **1940**, *8*, 212-224.

30. Lorenzo, A. T.; Arnal, M. L.; Albuerne, J.; Muller, A. J. Dsc Isothermal Polymer Crystallization Kinetics Measurements and the Use of the Avrami Equation to Fit the Data: Guidelines to Avoid Common Problems. *Polym. Test.* **2007**, *26*, 222-231.

31. Ishizuka, O.; Koyama, K. Crystallization of Running Filament in Melt Spinning of Polypropylene. *Polymer* **1977**, *18*, 913-918.

32. Martuscelli, E.; Pracella, M.; Crispino, L. Crystallization Behavior of Fractions of Isotactic Polypropylene with Different Degrees of Stereoregularity. *Polymer* **1983**, *24*, 693-699.

33. Pratt, C. F.; Hobbs, S. Y. Comparative Study of Crystallization Rates by Dsc and Depolarization Microscopy. *Polymer* **1976**, *17*, 12-16.

34. Avella, M.; Martuscelli, E.; Pracella, M. Low and High-Yield Isotactic Polypropylene - Isothermal Crystallization from the Melt. *J. Therm. Anal.* **1983**, *28*, 237-248.

35. Wei, Z. Y.; Zhang, W. X.; Chen, G. Y.; Liang, J. C.; Chang, Y.; Liu, L. A.; Wang, P.; Sun, J. C. Crystallization Behavior of Isotactic Polypropylene/Magnesium Salt Whisker Composites Modified by Compatibilizer Pp-G-Mah. *J. Therm. Anal. Calorim.* **2011**, *103*, 701-710.

36. Wei, Z. Y.; Zhang, W. X.; Chen, G. Y.; Liang, J. C.; Yang, S.; Wang, P.; Liu, L. A. Crystallization and Melting Behavior of Isotactic Polypropylene Nucleated with Individual and Compound Nucleating Agents. *J. Therm. Anal. Calorim.* **2010**, *102*, 775-783.

37. Zhu, X.; Yan, D. Influence of the Order of Polymer Melt on the Crystallization Behavior: Ii. Crystallization Kinetics of Isotactic Polypropylene. *Colloid Polym. Sci.* **2001**, *279*, 546-553.

38. Ponting, M.; Lin, Y.; Keum, J. K.; Hiltner, A.; Baer, E. Effect of Substrate on the Isothermal Crystallization Kinetics of Confined Poly(E-Caprolactone) Nanolayers. *Macromolecules* **2010**, *43*, 8619-8627.

39. Wang, H.; Keum, J. K.; Hiltner, A.; Baer, E. Crystallization Kinetics of Poly(Ethylene Oxide) in Confined Nanolayers. *Macromolecules* **2010**, *43*, 3359-3364.

40. Koh, Y. P.; Simon, S. L. Crystallization and Vitrification of a Cyanurate Trimer in Nanopores. *The Journal of Physical Chemistry B* **2012**, *116*, 7754-7761.

41. Hoffman, J. D.; Weeks, J. J. Melting Process and the Equilibrium Melting Temperature of Polychlorotrifluoroethylene. *J. Res. Natl. Bur. Stand., Sect. A* **1962**, *66A*, 13-28.

42. Sperling, L. H., *Introduction to Physical Polymer Science*. Wiley: 2005.

43. Yamada, K.; Hikosaka, M.; Toda, A.; Yamazaki, S.; Tagashira, K. Equilibrium Melting Temperature of Isotactic Polypropylene with High Tacticity: 1. Determination by Differential Scanning Calorimetry. *Macromolecules* **2003**, *36*, 4790-4801.

44. Yamada, K.; Hikosaka, M.; Toda, A.; Yamazaki, S.; Tagashira, K. Equilibrium Melting Temperature of Isotactic Polypropylene with High Tacticity. 2. Determination by Optical Microscopy. *Macromolecules* **2003**, *36*, 4802-4812.

45. Jackson, C. L.; Mckenna, G. B. The Melting Behavior of Organic Materials Confined in Porous Solids. *J. Chem. Phys.* **1990**, *93*, 9002-9011.

46. Lovinger, A. J.; Chua, J. O.; Gryte, C. C. Studies on Alpha and Beta Forms of Isotactic Polypropylene by Crystallization in a Temperature-Gradient. *J. Polym. Sci., Part B: Polym. Phys.* **1977**, *15*, 641-656.

47. Mark, J. E., *Physical Properties of Polymers Handbook*. Springer London, Limited: 2007.

48. Alizadeh, A.; Sohn, S.; Quinn, J.; Marand, H.; Shank, L. C.; Iler, H. D. Influence of Structural and Topological Constraints on the Crystallization and Melting Behavior of Polymers: 3. Bisphenol a Polycarbonate. *Macromolecules* **2001**, *34*, 4066-4078.

49. Jang, B. N.; Wilkie, C. A. The Thermal Degradation of Bisphenol a Polycarbonate in Air. *Thermochimica Acta* **2005**, *426*, 73-84.

50. Davis, A. Comparison of the Thermal and Thermo Oxidative Stability of Polycarbonate, Polyphenylene Oxide, Polysulphone and Two Polyarylates. *Die Makromolekulare Chemie* **1970**, *132*, 23-33.

51. Kremer, F., Broadband Dielectric Spectroscopy to Study the Molecular Dynamics of Polymers Having Different Molecular Architectures. In *Physical Properties of Polymers Handbook*, Mark, J., Ed. Springer New York: 2007; pp 385-393.

52. *Electrical Power Capacitors*. McGraw-Hill Education (India) Pvt Limited: 2001.

53. Tian, M.; Xu, S.; Wang, J.; Kumar, N.; Wertz, E.; Li, Q.; Campbell, P. M.; Chan, M. H. W.; Mallouk, T. E. Penetrating the Oxide Barrier in Situ and Separating Freestanding Porous Anodic Alumina Films in One Step. *Nano Letters* **2005**, *5*, 697-703.

APPENDIX: INSTRUMENTATION

Differential Scanning Calorimetry Theory

Differential scanning calorimetry can be used to measure thermal transitions and properties of a material. The instrument measures the change in the heat flow needed to raise the temperature of a sample with respect to a reference as a function of temperature and time. The heat flow and the ramping rate used to vary the temperature are related to the heat capacity through the following equation

$$\frac{dq}{dt} = C_p \frac{dT}{dt} \qquad (10)$$

where, *dq/dt* is the heat flow recorded, *dT/ dt* is the pre-set ramping rate and C_p is the heat capacity of the material. Figure 27 shows a schematic of the DSC set-up.

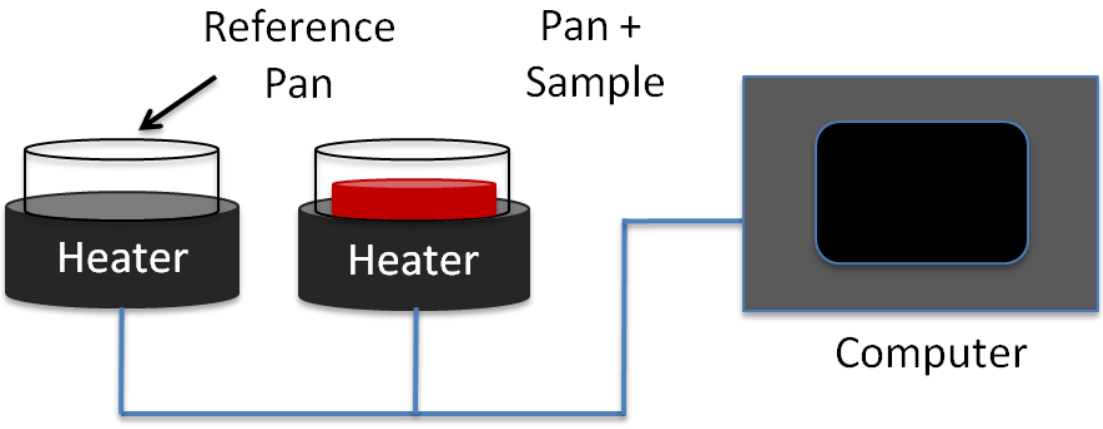

Figure 27. DSC schematic.

X-Ray Diffraction Theory

To analyze a material by x-ray diffraction an incident beam is aimed at the sample and the diffracted rays are collected by a detector. The gathered pattern of scattered x-rays provides information about the ordering and structure of the material. The angle formed between the incident beam and the diffracted beam is defines as the diffraction angle, 2θ. The diffraction angle is related to the spacing between crystallographic planes through the Braggs Law accordingly:

$$\lambda = 2d_{hkl}\sin\theta \qquad (11)$$

where, the x-ray wavelength, λ, is defined by the instrument, d_{hkl} is the spacing between planes and θ is the diffraction angle.